



Mechanistic stages of the SCR reaction – Insights into the trade-off between NO reduction and NH₃ oxidation over CuSSZ-13 catalysts via isotopic ¹⁵NH₃ and ¹⁸O₂ TPSR and steady state studies supported by IR 2D COS and DFT modeling

Monika Fedyna^a, Bartosz Mozgawa^a, Filip Zasada^a, Kinga Góra-Marek^a, Joanna Gryboś^a, Witold Piskorz^a, Chengyang Yin^b, Zhen Zhao^b, Piotr Pietrzyk^a, Zbigniew Sojka^{a,*}

^a Faculty of Chemistry, Jagiellonian University, ul. Gronostajowa 2, 30-387 Kraków, Poland

^b Institute of Catalysis for Energy and Environment, College of Chemistry and Chemical Engineering, Shenyang Normal University, Shenyang, Liaoning 110034, China

ARTICLE INFO

Keywords:

SCR mechanism
Ammonia oxidation
SCO
Cu-SSZ-13
Isotopic studies

ABSTRACT

Isotopic labeling investigations into SCR reaction were performed over CuSSZ-13 zeolites, obtained by one-pot synthesis or impregnation, and characterized by XRD, HR-SEM, TEM/EDX, EPR, and IR techniques. The course of SCR and internal ammonia oxidation (i-AMO) was revealed by isotopic TPSR and steady-state investigations using ¹⁵NH₃ and ¹⁸O₂ joined with IR Rapid Scan 2D-COS spectroscopy. The ¹⁴N¹⁵N and ¹⁵N₂ profiles allowed for quantification of the relative contributions of the concurrent SCR and i-AMO reactions. Interpretation of the results was ascertained by DFT and first-principles thermodynamic modeling. Three temperature regions of SCR reactions, corresponding to NH₃-rich, lean and dry conditions, were distinguished, and the main processes and intermediates involved in each stage were identified. For the conceptualization of SCR, a 2D diagram of the reactants and intermediates stoichiometry, oxidation state, and charge commensurability was constructed, and used for rationalization of the reaction mechanism.

1. Introduction

For the elimination of nitrogen oxides produced by Diesel engines, selective catalytic reduction with ammonia (NH₃-SCR) is widely applied [1–3]. This process is ubiquitously mingled with the ammonia slip problem, where excessive NH₃ unreacted with NO_x escapes with the exhaust gases, causing air pollution. Thus, development of efficient systems for the catalytic oxidation of ammonia to support the implementation of the NH₃-SCR technology is a closely related issue that needs to be addressed and resolved successfully [4,5].

Among many SCR systems explored so far, CuSSZ-13 zeolites are among the most active catalysts. The intricate nature of the SCR reaction, speciation and dynamics of the active sites, make copper chabazites attractive yet still challenging systems for both fundamental and applied studies [6–8]. Selective catalytic reduction of NO_x catalyzed by metal-zeolite materials is usually categorized into standard SCR and fast SCR when NO₂ is present [9]. Although the main steps of the low temperature NH₃-SCR mechanism over low loaded copper chabazites are

commonly acknowledged, specific mechanistic issues and molecular details are still debated and intensively investigated [10–13], particularly with respect to the involvement and role played by copper-oxo sites [14,15].

The temperature region of high NO_x conversion has been reported to be controlled by interrelated factors, such as copper loading and its intrazeolite speciation, the Si/Al ratio and Brønsted acidity [16–19]. Significant progress in mechanistic understanding has been achieved owing to decoupling of the SCR reaction into the reduction and reoxidation steps, constituting its essentially redox character [2,6,10]. The reduction half-cycle (RHC) is initiated by NO-assisted activation of the N–H bond of a NH₃ molecule coordinated by the Cu²⁺ centers; resulting in the formation of Cu⁺ cations and charge balancing protons (H⁺), along with the final N₂ and H₂O products. In the case of Cu²⁺–OH[–] centers, the N–N bond can be formed through HONO intermediates with copper reduction [12,20]. Subsequent oxidation half-cycle (OHC) occurs with participation of NO and O₂, to produce NO₃/NO₂ intermediates, revealed spectroscopically [21]. At low temperatures, mobile

* Corresponding author.

E-mail address: sojka@chemia.uj.edu.pl (Z. Sojka).

<https://doi.org/10.1016/j.apcatb.2022.122309>

Received 31 October 2022; Received in revised form 16 December 2022; Accepted 18 December 2022

Available online 20 December 2022

0926-3373/© 2022 Elsevier B.V. All rights reserved.

$\text{Cu}^+(\text{NH}_3)_2$ cage complexes are proposed to be involved in dioxygen activation and subsequent formation of NO_3/NO_2 species [7,22,23], which can react with $\text{NH}_3/\text{NH}_4^+$, regenerating the Cu^{2+} centers [21,24]. The remaining Brønsted trapped NH_3 (NH_4^+) can also participate in the reaction cycle under specific conditions [18,25]. These findings constitute a general mechanism of low-temperature NH_3 -SCR, which was found to be applicable to Cu zeolites containing predominantly isolated copper sites [26]. The high-temperature mechanism of SCR has been less explored, particularly for the CuSSZ-13 catalyst with a Si/Al ratio < 9 (typically used in commercial catalysts), despite its evidently good catalytic activity [8]. In addition to the Cu^{2+} and $\text{Cu}^{2+}\text{-OH}$ active sites, these catalysts exhibit a fraction of the $\text{Cu}^{2+}\text{-O}^{2-}\text{-Cu}^{2+}$ entities, which can participate in the SCR catalytic cycles [14,15], but also stimulate NO oxidation to NO_2 , which is beneficial for activating the fast SCR mechanism. In fact, an increase in the rate of NO to NO_2 oxidation has been observed with increasing amounts of the Cu_xO_y entities [27,28]. However, their mechanistic role in SCR and associated undesirable processes, such as NH_3 oxidation, has not yet been fully understood. Such centers gain in importance in the case of the copper zeolite catalysts obtained by solid-state exchange [29,30]. Unfortunately, the excessive formation of Cu_xO_y species observed at higher copper loadings leads to the enhanced hydrothermal deterioration of the catalysts (see [8] and references therein).

The course of SCR can be complicated by concomitant side oxidation of NH_3 and NO, which may occur in parallel or be interlaced with the primary reaction. Conventional SCR catalytic tests are of limited value in delineating of those reactions because the origin of dinitrogen atoms cannot be determined when isotopically unlabeled reactants are used. Instead, parallel oxidation of NH_3 is often used as a reference reaction to examine the ammonia oxidation capacity of the SCR catalysts, assuming that the results obtained are acceptably transferable into the mechanistic investigations of the SCR course [31,32].

NH_3 oxidation is often assumed to occur preferentially on encapsulated CuO clusters or on CuO particles segregated on the external surface of the zeolite catalyst [33,34]. The reaction involves multiple steps, where initially NH_3 reacting with O_2 (preferentially on the surface of CuO) generates NO_x species, which are then reduced by NH_3 to N_2 over the isolated Cu^{2+} cations housed in zeolite cages, following an internal selective catalytic reduction pathway (i-SCR) [4,33,35]. Alternatively, oxidation of ammonia may directly lead to dinitrogen via an imide mechanism [4,36]. In the light of the existing mechanistic ambiguities, further studies are needed to understand not only the prime SCR reaction mechanism, but also the possible accompanying processes that influence the overall catalyst SCR activity and selectivity.

The vast majority of SCR investigations have been performed in the steady-state regime, providing the core data on the reaction kinetics [6, 10,11,37,38]. Further mechanistic insight, not available from steady-state studies, has been obtained by transient, time-resolved isothermal experiments using the reactant mixtures of dedicated compositions in predefined sequences, which allow for probing the RHC and OHC steps separately [14,39–42]. However, when interpreting these results, it should be noted that such cut-off experiments significantly perturb the reaction conditions, which may strongly deviate from the real SCR circumstances.

To approach the dynamic conditions of real engine operation, where the temperature is changing abruptly and NH_3 is intermittently dosed to exhaust gases, temperature-programmed surface reaction (TPSR) techniques can be applied, providing complementary information on the dynamics of the SCR reaction [43,44]. The effects resulting from an uneven capture of the reactants by the active sites of the Cu-SSZ13 catalysts at varying temperatures can be probed in this test mode. Understanding the impact of the dynamic local disparities in the amount of the intra-cage NH_3 and NO reactants on the SCR reaction course, may provide unique information about catalyst operation in the cold start period under recurrent ammonia dosage [45,46].

The aim of this work was to use N-15 and O-18 labeling techniques to

clarify a trade-off between the primary SCR and the side reactions of ammonia oxidation or NO_x decomposition. We performed catalytic TPSR and steady-state studies using isotopically labeled $^{15}\text{NH}_3$ and $^{18}\text{O}_2$ reactants. This approach, supported by IR 2D COS and EPR spectroscopic studies, corroborated by DFT and ab initio thermodynamic modeling, allowed us to extract and quantify a selective reduction component from total NO conversion, and reveal the origin of the nitrogen atoms in N_2 and NO molecules produced in the course of simultaneous SCR and NH_3 oxidation processes.

Various unsteady state (TPSR) experiments designed in these studies, due to uneven accumulation of NH_3 and NO in the zeolite cavities, reflect dynamic conditions of the SCR process (variations in temperature and the NH_3/NO ratio), providing new mechanistic insights into the reaction network that are unavailable from isothermal steady-state experiments.

2. Experimental

2.1. Materials

The parent $\text{NH}_4\text{SSZ-13}$ zeolite with Si/Al = 7.9 (70% of single Al sites), synthesized as described previously [47,48], was obtained from Heyrovsky Institute in Prague. The XRD pattern confirmed its CHA structure and high crystallinity, while the ^{31}Si and ^{27}Al MAS NMR spectra proved the absence of extra-lattice aluminum species [49]. The corresponding CuSSZ-13 zeolite was obtained by impregnation with a CuCl_2 precursor (780 μmol of Cu/g of zeolite), and the sample was then dried at 100 °C and calcined at 700 °C for 2 h. As shown below, this preparation allowed for the intentional formation of all types of copper species (isolated Cu^{2+} and $\text{Cu}^{2+}\text{-OH}^-$, Cu-oxo clusters, and CuO nanoparticles), which are possibly involved in SCR and side NH_3 oxidation reactions. This sample is labeled i-CuSSZ-13, hereafter. The CuSSZ-13 sample with Si/Al = 4.7 was obtained by one-pot synthesis. In a typical procedure, 1.149 g of $\text{CuSO}_4\cdot 5\text{H}_2\text{O}$ was added to 0.514 g of NaAlO_2 diluted in 4.722 g of water, and the mixture was stirred at the 400 r/min rate for 0.5 h. Subsequently, 1.07 g of TEPA template and 0.69 g of NaOH (with efficient stirring) were introduced. Finally, 3.95 g of a silica sol (40 wt%) was added to the above mixture with efficient stirring at 800 r/min for 3 h. The resulting mixture was transferred to an autoclave and heated at 150 °C for 6 days. The solid product was collected by filtration, rinsed several times, and then dried at 100 °C for 12 h. The as-prepared Cu-SSZ-13 was then exchanged with NH_4NO_3 at 80 °C for 12 h, dried at 120 °C for 12 h, and finally calcined at 550 °C for 6 h. The obtained sample, containing 3.74 wt% of Cu, is free of segregated CuO nanoparticles (see below), and is hereafter labeled as o-CuSSZ-13.

2.2. Characterization methods

IR measurements were carried out with a Bruker Vertex 70 spectrometer, using self-supported pellets (5 $\text{mg}\times\text{cm}^{-2}$), which were placed in a quartz cell equipped with the CaF_2 windows. Prior to the experiments, the samples were dehydrated at 250 °C for 30 min under vacuum, and then upon admission of 60 Torr of oxygen heated at 550 °C for 1 h. The IR spectra (measured at -100°C) were normalized to the standard pellet mass (10 mg and 2.8 $\text{mg}\times\text{cm}^{-2}$ density). The integral intensities of the $\text{Cu}^{2+}(\text{CO})$ and $\text{Cu}^+(\text{CO})$ bands, were used for the titration of the accessible Cu^{2+} and Cu^+ species, applying the extinction coefficients equal to 0.11 $\text{cm}^2\times\mu\text{mol}^{-1}$ and 1.30 $\text{cm}^2\times\mu\text{mol}^{-1}$, respectively [50].

The chemical composition of the samples (Si, Al, Cu) was determined by means of inductively coupled plasma optical emission spectroscopy (iCAP 7400, Thermo Scientific).

Powder X-band EPR spectra were recorded at 77 K with a Bruker ELEXSYS-E500 spectrometer. Computer simulations were performed with the EPRsim32 program [51]. Prior to the EPR adsorption measurements, the samples were thermally activated under vacuum, then

heated in O₂ at 500 °C for 1 h, and finally outgassed. The samples were then saturated with NH₃ and/or NO and heated to desired temperatures. To probe the presence of reduced Cu⁺ centers, NO adsorption was carried out at 0 °C, to prevent side reactions between NO and the copper species.

High-resolution scanning electron microscopy (FE-SEM) imaging of the catalysts at the 1 kV acceleration voltage was performed on a Helios instrument (Thermo-Fisher), whereas conventional SEM measurements at the 30 kV acceleration voltage were carried out on a Tescan-Vega 3 microscope, equipped with the LaB₆ electron gun.

Analysis of the morphology and elemental composition of the samples was carried out by means of a FEI Tecnai Osiris (200 kV) microscope. Mapping of the constituent elements was achieved with energy dispersive X-ray spectroscopy (EDX), using a Super-X EDX windowless system with four-sector silicon drift detector (SDD), and the Bruker Esprit software.

2.3. TPD and catalytic measurements

Temperature-programmed desorption (TPD) experiments were carried out in a quartz fixed-bed reactor coupled with a QMS detector (Hidden Analytical HPR20). The total flow rate was 40 mL/min, and the mass of the zeolite samples (0.2–0.4 mm fraction) was 40 mg. Prior to the TPD measurements, the investigated samples were calcined in a 5% O₂/He flow at 500 °C (1 h) with a temperature ramp of 10 °C/min, and then cooled to 50 °C under He flow. NH₃ adsorption (1000 ppm in He) was performed for 1 h at 50 °C. Before desorption, the samples were purged with helium at the NH₃ adsorption temperature, and the TPD experiments were carried out from 50 °C to 650 °C, under He flow with a temperature ramp of 10 °C/min.

Catalytic tests of selective catalytic reduction and ammonia oxidation were carried out in the temperature-programmed surface reaction (TPSR) and isothermal modes, using a quartz fixed-bed reactor coupled with a quadrupole mass (Hidden Analytical) and an FTIR spectrometer with a multiple reflection gas cell of the 2 m path length. The total flow rate was 40 mL/min, and the mass of the zeolite samples (0.2–0.4 mm fraction) was 40 mg. Before catalytic measurements, the zeolites were calcined in 5% O₂/He flow at 500 °C (1 h). Catalytic tests were carried out under a flow of 500 ppm of ¹⁴NO (Linde), 500 ppm of ¹⁴NH₃ (Linde) or ¹⁵NH₃ (Eurisotop), and 4.5% of ¹⁶O₂ or ¹⁸O₂ (Oxford isotopes, 97% of O-18 enrichment) in He as a balance, without and with the presence of 3% of H₂O. The TPSR experiments were carried out from 50 °C to 500 °C under the flow of the SCR reactants with heating rate of 3 or 10 °C/min. The isothermal catalytic tests were carried out in a temperature range of 100–500 °C, until steady state was achieved (20–30 min). NH₃-AMO tests were performed under the same conditions, but without NO in the reaction mixture.

2.4. DFT and ab initio thermodynamic modeling

Spin-resolved projector-augmented plane wave DFT/PW91+U molecular modeling was performed with the VASP package. The Hubbard parameter $U = 4.0$ eV was used for Cu ions. The cutoff energy of 450 eV, the Methfessel-Paxton smearing parameter of $\sigma = 0.05$ eV, and the gamma-point sampling of the irreducible Brillouin zone were used. The geometry optimization criterion for the forces acting upon the ions was set at 10^{-4} eV/Å, while the SCF convergence criterion was set at 10^{-5} eV. Dispersion forces were treated within the Tkatchenko and Scheffler approach (DFT-TS). Calculations were performed with a hexagonal unit cell of the SSZ-13 zeolite ($a = b = 13.778$ Å, $c = 14.879$ Å), and the stoichiometry of O₇₂Si₃₄Al₂Cu. For optimization of unit cell size the Birch-Murnaghan equation was used. For periodic CuO modeling, the U parameter of 7 eV was applied [52]. The adsorption energies of NO, O₂, and NH₃ on the (111) surface of CuO were calculated using a slab model of the Cu₈₀O₈₀ stoichiometry and the ~ 9.5 Å thickness, with a vacuum layer of 10 Å (see Supporting Information). Transition-state

optimization was performed with the nudged elastic band method (NEB), using 5–9 NEB images (including the initial and final ones) for each calculated barrier.

First-principles thermodynamics (FPT) was applied to model the interaction of CuSSZ-13 zeolite with the reactants $X = \text{NO}, \text{NH}_3, \text{NO}_2$ under various conditions, following the method described previously [53]. The free enthalpy of the adsorption, as a function of T , p and the number of adsorbed molecules, was calculated as difference of the slab energy covered by the adsorbate and the chemical potential of gas molecules, $\mu(T, p_X)$. The latter was obtained from total DFT energy component (including the zero-point energy), and a part related to the variation of T and p_X via the perfect gas relationship.

3. Results and Discussion

3.1. Characterization of the CuSSZ-13 samples

The speciation of copper in the o-CuSSZ-13 and i-CuSSZ-13 catalysts was investigated by, microscopic (TEM/STEM/EDX, SEM), and spectroscopic (IR and EPR) techniques. The XRD patterns (Fig. S1, Supporting Information) confirm the CHA structure and good crystallinity of both catalysts, while the survey SEM analysis shows that the crystallites of both catalysts exhibit cubic-like shapes with the size of 1–2 μm for i-CuSSZ-13, and 1–0.5 μm for o-CuSSZ-13 (Fig. S2). However, in the case of the i-CuSSZ-13 catalyst, a more detailed low voltage HR-SEM examination, supported by high resolution STEM/HAADF/EDX (Fig. 1a₁–a₄), revealed the presence of small CuO nanocrystals ($\langle d \rangle \sim 4\text{--}5$ nm), segregated on the external surface of the zeolite grains (see Fig. 1b₁–b₃ and b₄ for the histogram of the CuO particle size). The results of the combined ultralow voltage HR-SEM (Fig. 1b₁) and HR-TEM (Fig. 1b₂) imaging imply that the small nanocrystals are located on the external surface, as the ellipsoidal cages of chabazite are too small ($6.7 \text{ Å} \times 11 \text{ Å}$) to accommodate even the smallest CuO grains (1 nm). The resolved (110) lattice fringes of a nanocrystal shown in Fig. 1b₃ confirm its tenorite structure (CuO). The EDX mapping proves an essentially even distribution of Al and Si, and the appearance of regions of an enhanced copper concentration, tantamount to the presence of the external CuO nanocrystals (Fig. 1a₂–a₄). Within the S/TEM resolution obtained, the presence of the encapsulated Cu_xO_y clusters could not be confirmed. However, their appearance is not excluded a priori, following EXAFS studies of CuSAPO-34 samples obtained also by the impregnation method [34].

Crystallites of the o-CuSSZ-13 catalyst exhibit a nearly cubic habit (Fig. 1c₁). The copper distribution is remarkably uniform and fully consistent with the spatial dispersion of Si and Al (Fig. 1c₂–c₄), without any features of segregated CuO entities. These observations confirm the presence of highly dispersed copper species, which are present only inside the chabazite cavities.

The speciation of copper into isolated Cu²⁺, Cu²⁺OH[−] and intra-zeolite copper-oxo entities was then examined by IR spectroscopy (using CO and NO as probe molecules). Adsorption of carbon monoxide under ambient conditions on CuSSZ-13 samples leads to the formation of various CO adducts with the exchanged copper cations (2230–2120 cm^{−1}). The monocarbonyl adducts with Cu²⁺ are characterized by higher stretching frequencies (2223 cm^{−1}), while the IR bands of CO at lower frequencies can be associated with the presence of Cu²⁺(OH)[−] species (2211 cm^{−1} and 2204 cm^{−1}) [54], monovalent Cu⁺ (2157 cm^{−1}), and Cu-oxo entities (2130 cm^{−1}). The corresponding IR spectra are shown in Fig. S3a, and the identified bands were used for the quantification of the intrazeolite distribution of copper into isolated Cu²⁺/Cu⁺ cations and Cu²⁺(OH)/Cu²⁺-oxo species (Table S1, Supporting Information), using the absorption coefficients published in [55]. The relative abundance of the Cu²⁺OH[−] species was additionally confirmed by analyzing the intensities of the corresponding bands at 3655 cm^{−1}. Their ratio approximately equal to 8 is close to the value determined using the CO probe (see Table S1). The presence of

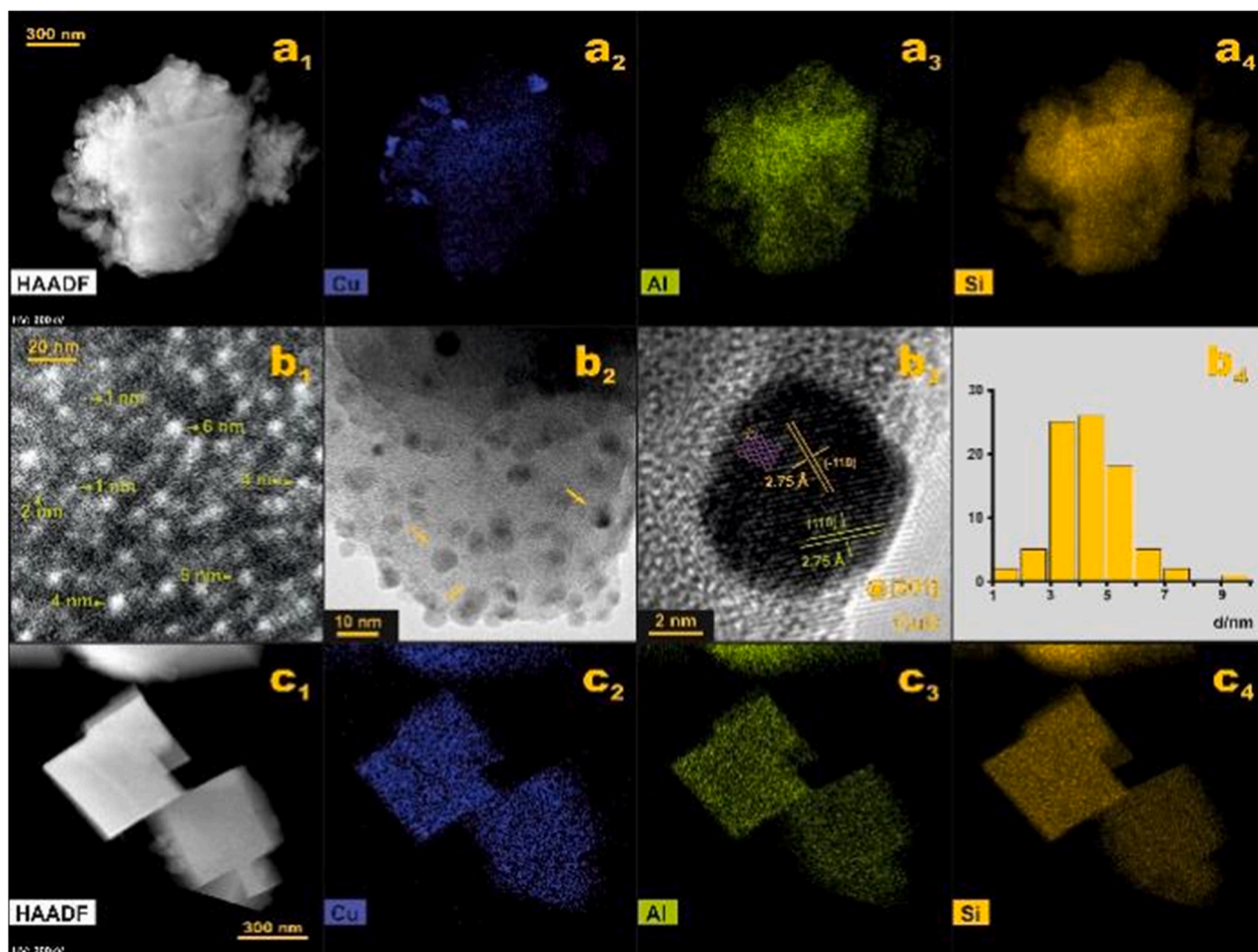


Fig. 1. STEM(a₁), HR-SEM (b₁), and HR-TEM (b₂, b₃) images of the i-CuSSZ-13 catalyst analog with the histogram of the CuO particle size distribution (b₄), and o-CuSSZ-13 catalyst (c₁), along with the corresponding EDX mapping of the Cu (a₂, c₂), Al (a₃, c₃) and Si (a₄, c₄) distributions.

copper-oxo entities in the o-CuSSZ-13 sample was independently revealed by in situ UV–vis measurements (Fig. S4), where apart from the dominant charge transfer peak at 213 nm, and d-d bands (below 600 nm) of copper, a band at 290 nm associated with Cu-O-Cu entities [56] can be distinguished.

For the assessment of an initial speciation of the intrazeolite Cu²⁺ cations among the 6MR and 8MR rings of the CHA structure, IR spectroscopy with NO acting as a probe molecule was used. The spectra obtained are shown in Fig. 2a,b, where the color coding of the deconvoluted peaks corresponds to a given type of the copper species. Their multiplicity results from inherent heterogeneity of the chabazite frameworks (different Si/Al ratios and Al distribution). As the individual speciation of Cu²⁺ cannot be assigned in a one to one fashion to the particular locus, based on these results, the component signals were combined into 3 generic classes of divalent copper located in the 6MR (σ or τ) and 8MR (τ) rings, and the copper oxo/CuO entities.

The analysis showed that in the case of the o-CuSSZ-13 sample, 53% of Cu²⁺ cations are located in the 6MR and 46% in 8MR rings, while for the i-CuSSZ-13 sample, 73% in the 6MR and 18% in the 8MR. The presence of the bands at 3615 cm⁻¹ and 3588 cm⁻¹, due to the Si(OH)Al groups located in the 8MR and D6R (hexagonal prism) sites, respectively, implies that part of the Brønsted sites (BAS) remains intact. For IR titration of the latter, ammonia was adsorbed at 150 °C under static conditions ($p_{\text{NH}_3} = 1.2\text{--}7$ Torr). For calculation of the total concentration of the Brønsted sites, the integral intensities of the 1450 cm⁻¹ bands of NH₄⁺, and the extinction coefficients of 0.11 cm² × μmol⁻¹ were used. The amount of residual Brønsted sites in o-CuSSZ-13 was equal to 603

μmol × g⁻¹, and 160 μmol × g⁻¹ for i-CuSSZ-13. The concentrations of all types of titrated copper and BAS species for both catalysts are summarized in Table S1.

The speciation of the isolated copper centers (Cu²⁺ and Cu²⁺-OH⁻) into 6MR (σ and τ) and 8MR (τ) sites, and their reducibility at various temperatures in the presence of NH₃, was next examined by EPR spectroscopy corroborated by computer simulation. Attribution of the component signals to the corresponding copper species was based on their spectroscopic signatures published previously [49]. Generally, the lower values of the *g*-tensor ($g_{\parallel} = 2.321\text{--}2.337$, $g_{\perp} = 2.062$) and the higher hyperfine splitting ($A_{\parallel} = 15.2\text{--}16.0$ mT) are diagnostic for Cu²⁺/8MR (τ), while the higher *g*-tensor values ($g_{\parallel} = 2.346\text{--}2.350$, $g_{\perp} = 2.063\text{e}$) and the lower hyperfine splitting ($A_{\parallel} = 14.5\text{--}14.9$ mT) correspond to Cu²⁺ in 6MR (σ). The results of the Cu quantification between the 8MR (τ) and 6MR (σ) sites are shown in Table S2. For the o-CuSSZ-13 sample, the isolated Cu²⁺ are initially nearly equally distributed (54% 6MR and 46% 8MR), while in the case of i-CuSSZ-13, a dominant part (80%) is located in the 6MR rings, and only 20% in the 8MR rings. Such site occupation remains in a very good agreement with the IR/NO titration results. With increasing temperature in the presence of ammonia, the copper cations located in the 8MR rings are more easily reduced than those located in the 6MR in both Cu-SSZ-13 samples (Table S2).

Spectroscopic characterization was complemented by NH₃-TPD studies (Fig. S5). NH₃ desorption profiles show three groups of broad peaks, the detailed interpretation of which has been described in our recent paper [49]. The distinct differences in the shape of the first band

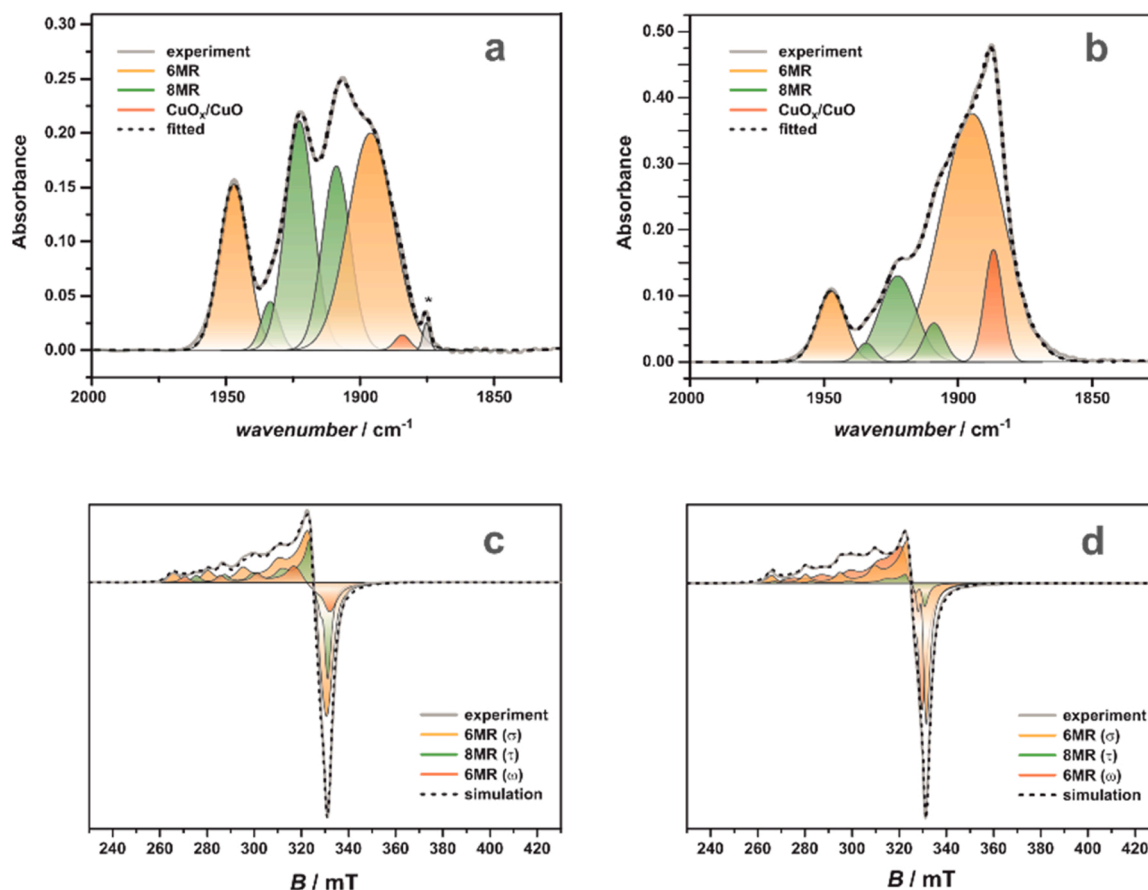


Fig. 2. Deconvoluted IR spectra of the NO region recorded at room temperature for the o-CuSSZ-13 (a) and i-CuSSZ-13 (b) catalysts, along with the EPR spectra recorded after thermal activation at 330 °C of the samples o-CuSSZ-13 (c) and i-CuSSZ-13 (d), with their decomposition into component signals.

are consistent with the lower abundance of the σ -Cu²⁺ and Cu²⁺OH⁻ centers along with an enhanced content of the τ -Cu²⁺ and BAS sites in the o-CuSSZ-13 sample compared to that of i-CuSSZ-13, in good agreement with the determined copper speciation. The second desorption band is associated with the release of NH₃ from divalent copper centers, whereas the third one from monovalent copper and BAS centers. The higher intensity of the band II and the lower intensity of band III are then consistent with the significantly higher reducibility of the i-CuSSZ-13 samples (Table S2). Interestingly, the TPD profiles reflect not only the differences in copper speciation, but also the fact that the desorption process is accompanied by partial oxidation of NH₃ into N₂ and NO (Fig. S6). In the temperature range of 100–170 °C the content of both oxidation products grows in parallel, but after passing 170 °C the production of N₂ increases abruptly, while that of NO decreases. Above 200 °C, the N₂/NO ratio is nearly constant, and is higher for the o-CuSSZ-13 sample than for i-CuSSZ-13. These observations indicate that NH₃ can be oxidized even in the absence of dioxygen over both types of the catalysts, which may be associated primarily with the presence of copper-oxo centers (NO formation), since CuO nanocrystals are absent in the o-CuSSZ-13 sample. In the case of o-CuSSZ-13, NO is produced in higher amounts compared to i-CuSSZ-13, implying a higher content of the copper oxo-species. The growth of N₂ always exceeds that of NO (see Fig. S6), suggesting that activation of the N–H bond (Cu²⁺–NH₃ + NH₃ → Cu⁺–NH₂ + NH₄⁺), which triggers subsequent formation of the N–N bond (through, e.g., the hydrazine route [57]) is feasible. The resulting Cu⁺–NH₂ species can also interact with autogeneously produced NO, giving rise to N₂ and H₂O, according to the noticeable increase in N₂ and a decrease in the level of the NO profile. These primarily conjectures are substantiated in more extensive experiments described below.

3.2. Evaluation of the NH₃-SCR performance

For disentangling the concurrent SCR and AMO reactions, isotopically labeled ¹⁵NH₃ and ¹⁸O₂ reactants were used for the TPSR studies. Such approach, can complement the information derived from the steady-state measurements. To reveal possible discrepancies in the reaction progress obtained in both modes, we compared the NO conversion profiles carried out isothermally in the steady-state regime (ITSS) and in the temperature-programmed transient fashion (TPSR). The results shown in Fig. S7 and discussed in Section 3, Auxiliary catalytic TPSR and IR spectroscopic results (Supporting Information), indicate that the NO conversion profiles obtained in the ITSS and TPSR modes are comparable for both catalysts in the region of high conversion, yet noticeable discrepancies related with adsorption/desorption of the reactants appear at low and high temperatures of the reaction.

In summary, while the steady-state catalytic measurements provide accurate kinetic data assessment about the catalyst activity and selectivity, the temperature-programmed mode uncovers those mechanistic features of the reaction that are naturally lost in the steady-state mode. The TPSR method allows for analysis of the concomitant adsorption and release of the reactants induced by the varying temperature, which appear significant for the catalyst performance and selectivity (see below). Due to the expensive isotopic gas expenditure, TPSR measurements were performed at the 10 °C/min heating rates, while the isotopic steady-state tests were carried out for representative temperatures only.

The temperature dependence and distribution of the products of the catalytic NO reduction and NH₃ oxidation during the NH₃-SCR and NH₃-AMO reactions, performed in the temperature-programmed fashion over the o-CuSSZ-13 and i-CuSSZ-13 catalysts, are shown in Fig. 3.

The NH₃ profiles recorded during the SCR reaction (Fig. 3a₁) show

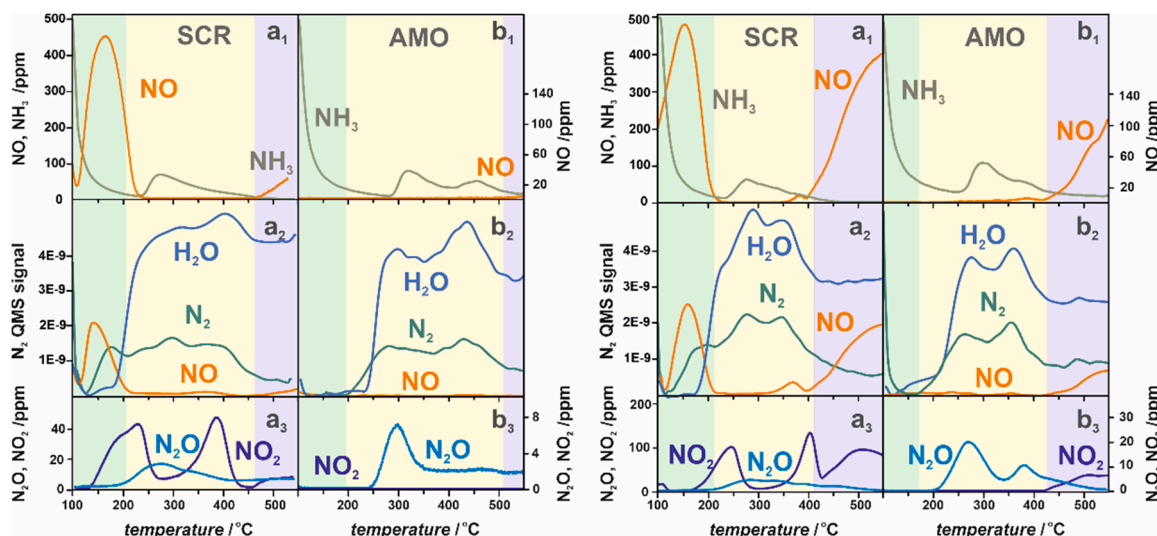


Fig. 3. TPSR profiles of the SCR ($\text{NO} + \text{NH}_3 + \text{O}_2$) reaction (a_1 – a_3) and AMO ($\text{NH}_3 + \text{O}_2$) reaction (b_1 – b_3) on the catalysts o-CuSSZ-13 (left panels) and i-CuSSZ-13 (right panels).

that in both samples the ammonia concentration decays rapidly below 200 °C, but in the temperature range of the highest NO conversion (200–450 °C), a part of NH_3 is desorbed, reaching the level of ~70 ppm with the local maximum appearing at ~270 °C. In the reference ammonia oxidation reaction (AMO) on the o-CuSSZ-13 zeolite, NH_3 desorption becomes bimodal, with the peaks occurring at 320 and 450 °C. They are shifted to 300 and 380 °C for i-CuSSZ-13 (Fig. 3b₁). In the SCR tests, NO is initially adsorbed, but with increasing temperature it rapidly desorbs with a peak maximum located already around 150 °C for both catalysts (Fig. 3a₁–a₂). In the case of o-CuSSZ-13, the region of the apparent full extinction of NO extends from 200° to 470°C, and then its concentration starts to steadily increase to ~ 60 ppm at 550 °C (Fig. 3a₂, left panel), in contrast to i-CuSSZ-13 where it rises dramatically to almost 400 ppm (right panel). However, it should be noted that at low temperatures, the NO removal due to the SCR reaction is disguised by the concomitant NO desorption, which leads to an artificial lowering of the conversion in the TPSR tests (see Fig. S7). The NO profiles recorded during the reference NH_3 -AMO reaction show that NO practically does not appear over the o-CuSSZ-13 catalyst in the whole temperature range, while for i-CuSSZ-13 it reaches a level of 100 ppm at 550 °C. The latter value is four times lower than in the SCR reaction (Fig. 3b₂, right and left side panels).

The evolution of N_2 during the SCR reaction shows a markedly different behavior compared to NO. This is particularly apparent in the temperature range of 200–400 °C, where the NO conversion is close to 100%. Several distinct local maxima of excessive N_2 production can easily be observed for both catalysts (Fig. 3a₂, right and left side panels), showing that the NO conversion is not fully congruent with the N_2 production. The latter process evidently exhibits a more complex course, depending on the nature of the active sites and the reaction temperature. For o-CuSSZ-13, the production of N_2 starts above 110 °C, and passes through 4 intermittent maxima at 170 °C, 250 °C, 300 °C, and 400 °C, decaying with a clear inflection point at ~450 °C. The concurrent evolution of H_2O generally parallels the N_2 profile with the exception of the lowest temperatures, where water molecules apparently are still trapped within the zeolite channels (Fig. 3a₂, left). In the case of i-CuSSZ-13, in turn, a 3-modal profile of the N_2 evolution is observed, with the positions of the maxima appearing at 170 °C, 270 °C and 350 °C (Fig. 3a₂, right). The formation of N_2 in the course of the reference AMO reaction starts around 150–200 °C, exhibiting a bimodal character in both cases, with the maxima appearing at 270 °C and 420 °C (o-CuSSZ-13) and 250 °C and 350 °C (i-CuSSZ-13). Interestingly, NH_3 is partly desorbing around 300 °C, which may be responsible for the appearance of a “sea-

gull features” in the N_2 profile. The N_2 maxima in the AMO profile coincide with some of the N_2 peaks observed during SCR, suggesting that part of the irregularities in the N_2 formation can be traced back to the concomitant oxidation of NH_3 , which accompanies the primary NO reduction process. The excessive production of N_2 may result from the storage of NH_3 (in the Cu and BAS centers) or NO (in the form of nitrates) within the cages of the catalysts, as discussed in more detail below.

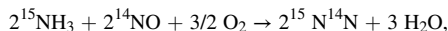
The corresponding changes in NO_2 and N_2O concentrations with temperature exhibit a much more dramatic character, which clearly depends on the speciation of copper. The strongly non-monotonic evolution of NO_2 shows that nitrogen dioxide is already produced at the beginning of the reaction, reaching the level of ~100 ppm for i-CuSSZ-13 and 40 ppm for o-CuSSZ-13. Apparently, NO_2 is next consumed in the temperature window of the highest NO conversion, promoting the fast SCR pathway (f-SCR), reappearing at ~350–400 °C (Fig. 3a₃). Above 450 °C the NO_2 concentration is becoming very low for o-CuSSZ-13 (< 10 ppm), in contrast to the i-CuSSZ-13 sample (70–80 ppm), where another broad maximum at 500 °C appears. This observation can be associated with the presence of CuO nanocrystals, as for o-CuSSZ-13 the NO_2 level is quite low. In the parallel NH_3 -AMO reaction, NO_2 is not produced over the o-CuSSZ-13 catalyst, but its small amounts (< 10 ppm) could be distinguished over the i-CuSSZ-13 zeolite above 400 °C. This indicates that most of the NO_2 results from NO oxidation over the CuO at such conditions.

Formation of N_2O is less important in all cases examined. It is produced most extensively during NH_3 oxidation over the i-CuSSZ-13 zeolite (< 20 ppm), with the main maxima located around 270 °C and 380 °C. They appear to be correlated with maxima in the N_2 profiles of the NH_3 oxidation reaction (Fig. 3b₃).

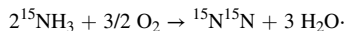
All the findings described above confirm that different mechanistic pathways are responsible for the observed irregularities in the formation of N_2 at low (first maximum) and at medium (second and third maximum) temperatures of the highest NO conversion. NO formation in the high temperature stage of the SCR reaction reaches the level of 400 ppm for i-CuSSZ-13, while in the AMO process it drops to ~100 ppm at 550 °C. It indicates that the loss of NO conversion in the SCR may only be partially explained by the oxidation of NH_3 to NO, provided that the AMO results can directly be transferred to the SCR context, when the concentration levels of NH_3 and O_2 are the same. This issue was addressed in more detail by using the isotopically labeled reactants.

3.3. Isotopic TPSR studies

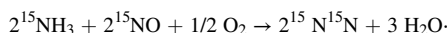
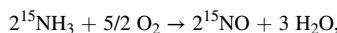
To give a more in-depth insight into the course of the SCR reaction, the TPSR experiments with labeled $^{14}\text{NH}_3$ and $^{18}\text{O}_2$ were next performed, and the results are collated in Fig. 4. Ammonia N-15 labeling was used for monitoring the origin of N_2 formation during the SCR process:



and its trade-off with the concurrent $^{15}\text{NH}_3$ oxidation:



The latter reaction most likely can proceed along an internal SCR route, where NO initially produced by NH_3 oxidation is then transformed into N_2 , directly or via nitrate/nitrite intermediates:



The temporal decline of NO in the exit gas mixture may also be associated with its oxidation to NO_2 and/or storage in the form of $\text{NO}_3^-/\text{NO}_2^-$ adspecies. These processes were followed using O-18 labeled dioxygen, in the SCR reaction carried out with the application of regular N-14 and N-15 enriched ammonia. However, the fact that $^{15}\text{N}_2$ and $^{14}\text{N}^{16}\text{O}$ (NO), as well as $^{14}\text{N}^{18}\text{O}$ and $^{16}\text{O}_2$, form isobars restricts the

information content of the corresponding profiles. Nevertheless, some useful mechanistic information can still be extracted from the experimental data when the analysis of the isotopic results is restricted to specific temperature regions where one of the isobars dominates, and analysis is supported by auxiliary experiments. Because the nitric oxide that enters with the gas feed is unlabeled, the SCR reaction performed with $^{15}\text{NH}_3$ (Fig. 4a,a₁, respectively) resolves the multimodal N_2 profile, observed with the unlabeled reactants (Fig. 3a₁), into the particular contributions coming from the SCR and AMO reactions. They are simply gauged by the content of the $^{14}\text{N}^{15}\text{N}$ and $^{15}\text{N}_2$ products, respectively. However, because $^{15}\text{N}_2$ and NO are indistinguishable by QMS, the former is diagnostic for the progress of AMO only in the temperature range of virtually full conversion of NO (marked in yellow).

An inspection of the initial fragments of the $^{14}\text{N}^{15}\text{N}$ profiles (Fig. 4a, a₁ - green line) shows that up to 200 °C, they exhibit similar shapes with the maxima located at virtually the same temperature for both catalysts. In this region, the SCR reaction is not perturbed by the AMO process, which is only launched above ~210 °C. This can be inferred from the steep increase in the $^{15}\text{N}_2$ line upon passing into the region of practically complete NO conversion (yellow area), where the contribution of N^{16}O to the $^{15}\text{N}_2$ signal can be safely neglected. In this temperature window, the $^{14}\text{N}^{15}\text{N}$ maximum is moved a bit toward higher temperatures for o-CuSSZ-13, and the high NO conversion is persistent until 550 °C, in contrast to the i-CuSSZ-13 sample (Fig. 4a,a₁). A more distinct difference can be seen in the shape of the $^{15}\text{N}_2$ AMO profiles (Fig. 4a,a₁). The initial increase in NH_3 oxidation above 200 °C is quite similar for both

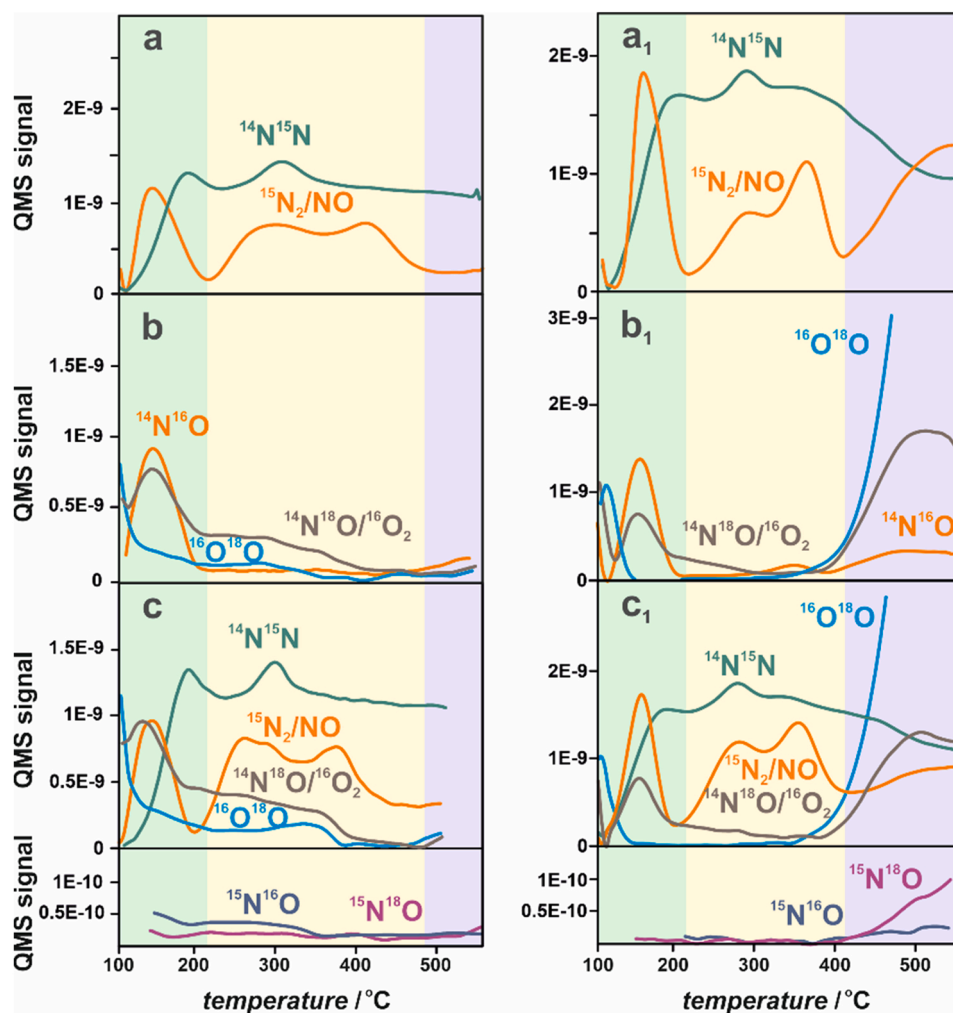


Fig. 4. TPSR profiles recorded during the isotopic SCR reaction over o-Cu-SSZ-13 catalyst (a-c, left panel) and i-Cu-SSZ-13 (a₁-c₁, right panel) catalyst using $^{16}\text{O}_2 + ^{15}\text{NH}_3$ (a, a₁) and $^{18}\text{O}_2 + ^{14}\text{NH}_3$ (b, b₁) and $^{18}\text{O}_2 + ^{15}\text{NH}_3$ (c, c₁) as reactants.

catalysts, but an increase in the $^{15}\text{N}_2$ production occurs around 350 °C for i-CuSSZ-13, while it is rather modest for o-CuSSZ-13. In the high temperature region (marked violet), a pronounced development of NO occurs only over the i-CuSSZ-13 catalyst, as already observed in the TPSR tests with the unlabeled reactants (Fig. 3).

The experiments with $^{18}\text{O}_2$ shed additional light on the nature of the changes in the SCR/AMO reactions throughout the increasing temperature. There is an interesting difference in the evolution of the $^{14}\text{N}^{16}\text{O}$ and $^{14}\text{N}^{18}\text{O}/^{16}\text{O}_2$ profiles for both catalysts (Fig. 4b,b₁,c,c₁). The initially adsorbed $^{14}\text{N}^{16}\text{O}$ is already released at the beginning, and is then rapidly consumed in the SCR reaction above ~150 °C. The $\text{N}^{18}\text{O}/^{16}\text{O}_2$ profile follows the general trend of NO variation at low temperatures, but the proportions of $^{14}\text{N}^{16}\text{O}$ and $^{14}\text{N}^{18}\text{O}/^{16}\text{O}_2$ are different for both catalysts. For i-CuSSZ-13, a comparison of the $^{14}\text{N}^{16}\text{O}$ and $^{14}\text{N}^{18}\text{O}/^{16}\text{O}_2$ profiles shows that 30–40% of NO, desorbed in the temperature range of 100–200 °C, corresponds to $^{14}\text{N}^{18}\text{O}/^{16}\text{O}_2$. These proportions are more balanced for the o-CuSSZ-13 sample. There is also a clear difference in the shape of the $^{14}\text{N}^{18}\text{O}/^{16}\text{O}_2$ curves in the 200–400 °C window, where nitric oxide conversion is the highest. An apparent similarity in the development of $^{14}\text{N}^{18}\text{O}/^{16}\text{O}_2$ and $^{16}\text{O}^{18}\text{O}$, implies that $^{16}\text{O}_2$ contributes significantly to the $m/z = 32$ line. Thus, $^{16}\text{O}^{18}\text{O}$ and $^{16}\text{O}_2$ together with $^{14}\text{N}^{18}\text{O}$ are produced from $^{18}\text{O}_2/^{14}\text{N}^{16}\text{O}$ by isotopic exchange over NO_3/NO_2 species, which are more abundant in the o-CuSSZ-13 sample than in i-CuSSZ-13 (see the reference IR spectra in Fig. S8).

These results indicate that in the course of the SCR reaction, nitrates/nitrites coexist with the copper-ammonia cage complexes, possibly both as separate species and in the form of mixed ligand adducts already at the low temperature stage. Noting that nitrates can be produced in the oxidized sample (Fig. S8), NO reduction can, therefore, embark along a normal and reversed way, i.e., starting from Cu-NH_3 or Cu-NO_3 intermediates. However, the most dramatic differences in the SCR reaction products are observed in the high temperature range, where the $^{14}\text{N}^{18}\text{O}/^{16}\text{O}_2$ line for i-CuSSZ-13 is becoming much more intensive than that of $^{14}\text{N}^{16}\text{O}$, in contrast to o-CuSSZ-13. The $^{16}\text{O}^{18}\text{O}$ isotopomer that appears already at the beginning of the reaction for i-CuSSZ-13 (Fig. 4b₁) is then nearly depleted at temperatures 100–150 °C, rising steeply above 380 °C (together with $^{14}\text{N}^{18}\text{O}$). In contrast, for o-CuSSZ-13 it is quite weak in the high temperature range, being distinctly stronger below 350 °C, similar to the $\text{N}^{18}\text{O}/^{16}\text{O}_2$ line. This behavior suggests a different origin for the formation of N^{18}O , $^{16}\text{O}_2$, and $^{16}\text{O}^{18}\text{O}$, depending on the temperature and the nature of the active copper sites dominant in the two types of the investigated catalysts. The high rate of $^{16}\text{O}^{18}\text{O}$ production on the i-CuSSZ-13 sample at $T > 380$ °C is clearly related to an isotopic exchange on the surface of the segregated CuO nanocrystals that are absent in o-CuSSZ-13 (see Fig. 1). It clearly proves an effective activation of dioxygen above 380–400 °C, which triggers an excessive external NH_3 oxidation (e-AMO) on CuO outside of the zeolite cage. The temperature evolution of $\text{N}^{18}\text{O}/^{16}\text{O}_2$ profile below 380–400 °C, in turn, can be related to the transformation of copper nitrates/nitrites associated with the $\text{Cu}^{2+}\text{-O}^{2-}\text{-Cu}^{2+}$ sites, where $^{18}\text{O}_2$ oxygen can also be exchanged into O-16. In fact, these centers are more abundant in the o-CuSSZ-13 sample (Table S1), and are involved in the internal NH_3 oxidation (i-AMO). In particular, in a reference experiment of NO interaction with $^{18}\text{O}_2$ over i-CuSSZ-13, analogous $^{16}\text{O}^{18}\text{O}$ and $^{14}\text{N}^{18}\text{O}/^{16}\text{O}_2$ profiles can also be distinguished, with the $^{14}\text{N}^{18}\text{O}$ maximum around 150 °C, and an abrupt rise of the $^{16}\text{O}^{18}\text{O}$ and $^{14}\text{N}^{18}\text{O}$ isotopomers above 380–400 °C (Fig. S9). The changes in $^{14}\text{N}^{18}\text{O}$ formation are roughly correlated with the NO_2 evolution (blue line), confirming that NO that passes through the catalyst bed in the presence of dioxygen is readily oxidized over the intrazeolite copper-nitrate centers. Above 400 °C, the oxidation is reinforced by external processes occurring on the segregated CuO nanocrystals, but under such conditions NO_2 becomes thermodynamically unstable and decomposes back into NO and O_2 . The fact that the $^{16}\text{O}^{18}\text{O}$ signal is rising steeply, while that of $^{14}\text{N}^{18}\text{O}$ saturates at high temperatures (Fig. S9, Fig. 4), indicates that

part of the dioxygen adsorbed in a dissociated way is exchanged on the CuO surface without involvement of the nitrate/nitrite intermediates.

The TPSR experiments were then repeated using isotopically labeled $^{18}\text{O}_2$ and $^{15}\text{NH}_3$ reactants simultaneously. In this case, the $^{15}\text{N}^{18}\text{O}$ and $^{15}\text{N}^{16}\text{O}$ isotopomers produced during the reaction unambiguously confirm the $^{15}\text{NH}_3$ oxidation to nitric oxide in the regions, where the $^{15}\text{N}_2$ signal is mixed with that of the $^{14}\text{N}^{16}\text{O}$ isobar (Fig. 4c,c₁). The $^{14}\text{N}^{16}\text{O}/^{15}\text{N}_2$ profile in the full conversion window (Fig. 4c,c₁) is essentially dominated by $^{15}\text{N}_2$, being again diagnostic for the concomitant ammonia oxidation. The $^{14}\text{N}^{18}\text{O}/^{16}\text{O}_2$ and $^{16}\text{O}^{18}\text{O}$ profiles (Fig. 4c, c₁) approve the general behavior of both catalysts revealed in the experiments with $^{18}\text{O}_2$ alone (Fig. 4b,b₁). However, in the high temperature region, simultaneous appearance of the signals due to the $^{15}\text{N}^{18}\text{O}/^{15}\text{N}^{16}\text{O}$, $^{14}\text{N}^{18}\text{O}$, and $^{14}\text{N}^{16}\text{O}$ isotopomers provides a direct evidence for the contribution of an intact NO, a nitric oxide passed over the nitrate/nitrite cycle, and NO derived from the ammonia oxidation to the observed changes in the nitric oxide profile, and the related loss of the selectivity of the i-CuSSZ-13 catalyst (Fig. 3a₁,b₁). Therefore, the simultaneous use of $^{15}\text{NH}_3$ and $^{18}\text{O}_2$ is indispensable here. As a result, the $^{14}\text{N}^{18}\text{O}/^{16}\text{O}_2$ traces can detect sensibly interaction of the cage nitrate intermediates with NO under the reaction conditions, which is essential for beneficial transformation of nitrates into nitrites. The isotopic TPSR studies of the SCR reaction were next repeated in the steady-state mode for both samples.

Isothermal catalytic measurements were performed at intermittent temperatures of 250 °C and 350 °C, after prior contact of the catalysts with the SCR reactants at 50 °C, and in a second experiment at 250 °C. In both cases, the catalysts were finally heated to 550 °C in the flow of O_2/He in order to reveal desorption of the remaining SCR products. The applied temperature ramps are shown in Fig. 5a,b.

Analysis of the thermal evolution of the NO curves shows that for all investigated conditions nearly complete NO conversion (solid orange line) was achieved in steady state after ~30 min of the reaction. The corresponding $^{14}\text{N}^{15}\text{N}$ and $^{15}\text{N}_2$ profiles confirm that the SCR reaction is always accompanied by the NH_3 oxidation. For o-CuSSZ-13 contacted with the reactants already at 50 °C, after reaching steady state at 190 °C, the contribution of NH_3 oxidation to its total conversion is equal to $p(^{15}\text{N}_2)/[p(^{15}\text{N}_2) + p(^{15}\text{N}^{14}\text{N})] \times 100\% = 15\%$, and increases to 25% at 300 °C. In the case of the same sample contacted with the reactants at 250 °C, the oxidation of ammonia is significantly lower (11%), increasing to 15% only at 350 °C. The results also show that the extent of NH_3 oxidation is clearly related to its local concentration (an actual cage NH_3/NO stoichiometry, disequibrated by different capture of both reactants by copper and BAS centers). A virtually complete conversion of NO (orange line) implies a strong domination of the SCR reaction, because the oxidized ammonia comes primarily from the excessive NH_3 molecules. This is coherently illustrated by the fact that NH_3 desorption maxima appearing during the heating stage (gray dotted lines) are well correlated with the maxima in the $^{15}\text{N}_2$ profiles (Fig. 5a,b), while the corresponding maxima of $^{14}\text{N}^{15}\text{N}$ (SCR) are barely visible (and only in the case of the temperature ramp of 190–300 °C, see Fig. 5a). Therefore, NH_3 molecules released from the coordination sphere of the single Cu^{2+} or $\text{Cu}^{2+}\text{-OH}^-$ centers in the windows of increasing temperature, can be relocated within the chabazite cavity, allowing their intrazeolite oxidation (i-AMO). It occurs preferentially on the $\text{Cu}^{2+}\text{-O}^{2-}\text{-Cu}^{2+}$ sites (see below). In our previous studies we have shown that dual the $\text{Cu}^{2+}\text{-O}^{2-}\text{-Cu}^{2+}$ sites liberate NH_3 molecules at lower temperatures than the isolated single Cu^{2+} or $\text{Cu}^{2+}\text{-OH}^-$ species, apparently the latter may then act as ammonia storage centers for the dual copper-oxo sites [49]. Analogous results were observed for i-CuSSZ-13, where again an increase in the temperature from 250° to 350°C triggers NH_3 release, which next gives rise to the associated enhancement of the ammonia oxidation (Fig. 5c). The fraction of oxidized ammonia is equal to 11% and 6% at 250 °C, and increases to 15% and 12% at 350 °C, for the o-CuSSZ-13 and i-CuSSZ-13 catalysts, respectively. There is a noticeable difference in the NH_3/N_2 profiles between the catalysts saturated with

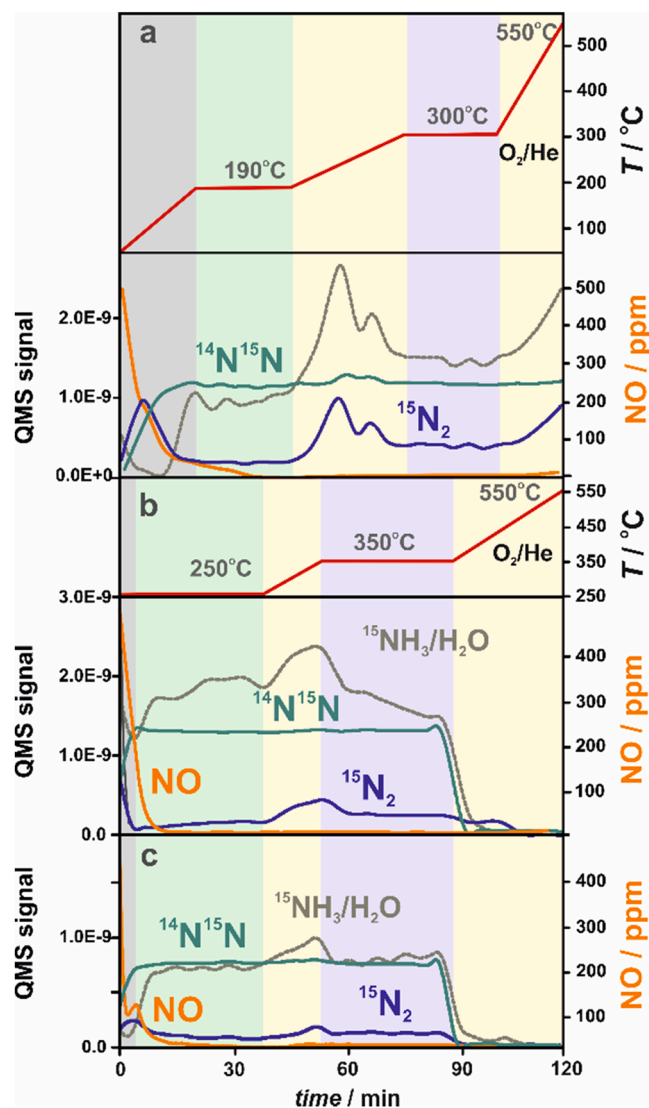


Fig. 5. Isotopic profiles recorded during the isothermal SCR reaction using $^{16}\text{O}_2 + ^{15}\text{NH}_3$. The test was performed after contact of the o-CuSSZ-13 catalyst with the reactants at 50 °C, and next isothermally at 190 °C and 300 °C (a), or upon contact with the o-CuSSZ-13 (b) and i-CuSSZ-13 (c) catalysts with the reactants at 250 °C with isothermal measurements at 250 °C and 350 °C. In all cases, after the isothermal tests, the catalyst was subsequently heated to 550 °C in the flow of O_2/He .

the reactants at 50 °C and 250 °C, after the cut-off of the reactants and subsequent heating of the samples in O_2/He till 550 °C. A clear development of NH_3 and N_2 results from desorption and partial oxidation of ammonia, stored in the bulk of the zeolite during saturation at 50 °C prior to the reaction at 190 °C (Fig. 5a, broad gray stripe). For the samples exposed immediately to the reaction temperature of 250 °C (Fig. 5b, narrow gray stripe), the storage of ammonia in the bulk is dramatically reduced. As a result, only some residual NH_3 and N_2 species evolve after the cut-off of the reactants as the temperature increases to 550 °C in O_2 .

These results clearly show that local excess of gaseous NH_3 in the zeolite cage promotes ammonia oxidation in the course of the SCR reaction. All these issues are discussed comprehensively on the basis of the results of the corroborative DFT/FPT modeling in the next sections. The effect of water, though beyond the intended scope of this work, is briefly addressed in Section 4, *Effect of water on SCR and AMO reactions* (Supporting Information).

3.4. IR studies of formation, stability and reactivity of AMO and SCR intermediates

To support interpretation of the isotopic TPSR and steady-state results, we investigated the interaction of NO, NH_3 , and O_2 adsorbed in various combinations by means of standard IR and Rapid Scan IR 2D COS spectroscopy (complementary results and their discussion are described in Section 5, *IR investigations of NH_3 oxidation* (Supporting Information)).

3.4.1. IR studies of NH_3 oxidation

Upon adsorption of NH_3 at room temperature, the IR spectra of both samples are dominated by the bands at 1623 cm^{-1} , attributed to $\delta(\text{NH}_3)_{\text{asym}}$ vibrations of the $\text{Cu}^{2+}\text{-NH}_3$ adducts [18,19,49], and at 1445 cm^{-1} (Fig. S12), assigned to distal NH_4^+ (NH_3 adsorption on BAS) [49]. In the presence of O_2 , upon increasing the reaction temperature, a part of the coordinated NH_3 is detached ($\sim 150\text{ }^\circ\text{C}$), whereas the bands at 1623 cm^{-1} and 1445 cm^{-1} are distinctly shifted and their shapes are noticeably changed. Following the detailed analysis of these bands, supported by the 2D COS spectra presented in Section 5 (Supporting Information), we think that apart from copper ammonia adducts, copper nitrates, and possibly also mixed ligand adducts may reasonably contribute to development of the observed evolution of the complex band around 1623 cm^{-1} [58,59], whereas the shoulder appearing at 1428 cm^{-1} can be associated with the formation of proximal NH_4^+ [60] and/or nitrosamine species [61], produced during the reaction.

These observations can be epitomized as follows. Oxidation of NH_3 occurs through formation of the proximal NH_4^+ species ($\text{Cu}^{2+}\text{-NH}_3 + \text{NH}_3(\text{cage}) \rightarrow \text{Cu}^+\text{-NH}_2 + \text{NH}_4^+$). Such reaction requires the participation of a cage NH_3 molecule (according to the isotopic results) as oxidation of NH_3 is well correlated with the release of NH_3 into the zeolite cavities (see Fig. 5). The resulting $\text{Cu}^+\text{-NH}_2$ species can be oxidized by O_2 into NO ($\text{Cu}^{2+}\text{-NH}_2 + \text{O}_2 \rightarrow \text{Cu}^+\text{-NO} + \text{H}_2\text{O}$), and next in the presence of O_2 into $\text{NO}_3^-/\text{NO}_2^-$ or react with NO to produce the nitrosamine adduct ($\text{Cu}(\text{H}_2\text{-N}=\text{O})$ [12,62]. This creates a molecular backbone for the operation of the internal SCR as a possible pathway of ammonia oxidation [32, 35,63]. As a result, we can sensibly assign the characteristic feature around 1428 cm^{-1} to the proximal NH_4^+ and/or $\text{O}=\text{N-NH}_2$ species, produced from the H^+ and $-\text{NH}_2$ moieties of the ammonia dissociation, upon their interaction with NH_3 (AMO) and NO (SCR/i-SCR), respectively.

Analysis of the high frequency region of $3500\text{--}3800\text{ cm}^{-1}$ reveals another route along which the NH_3 molecule is activated (Fig. S12a₁, b₁). Changes in the intensity of the 3658 cm^{-1} peak ($\text{Cu}^{2+}\text{-OH}^-$) with concomitant increase in the H_2O band at 3640 cm^{-1} above $150\text{ }^\circ\text{C}$, can be reconciled with the following reaction, $\text{Cu}^{2+}\text{-OH}^- + \text{NH}_3(\text{cage}) \rightarrow \text{Cu}^+\text{-NH}_2 + \text{H}_2\text{O}$. Dissociative insertion of an NH_3 molecule into the di-copper oxo species provides an additional conceivable way to activate the N-H bond ($\text{Cu}^{2+}\text{-O}^{2-}\text{-Cu}^{2+} + \text{NH}_3(\text{cage}) \rightarrow \text{Cu}^+\text{-NH}_2 + \text{Cu}^{2+}\text{-OH}^-$), which accounts for reappearance of the $\text{Cu}^{2+}\text{-OH}^-$ species at higher temperatures (Fig. S12a₁). These two processes initiate the partial transformation of NH_3 into N_2/NO , observed already in the mere NH_3 -TPD experiments (see Fig. S6). The thermodynamic and kinetic analysis of those three possible routes of dissociation of the N-H bond is discussed below.

3.4.2. Interaction of the catalysts with the SCR reactants

The IR spectra recorded at the milestone temperatures of the interaction of CuSSZ-13 catalysts with the SCR reactants (NO, NH_3 , and O_2) are shown in Fig. 6.

The IR spectrum of o-CuSSZ-13 contacted with the SCR reactants at $150\text{ }^\circ\text{C}$ (Fig. 6a) is dominated by the strong bands around 1621 cm^{-1} and $1440\text{--}1450\text{ cm}^{-1}$ discussed above. The situation appears different for the i-CuSSZ-13 catalysts (Fig. 6b), where the band around $1440\text{--}1450\text{ cm}^{-1}$ is weak, and the bands due to N_2O (2224 cm^{-1}) and NO^+ (2173 cm^{-1}) appear already at $150\text{ }^\circ\text{C}$, with the maximum

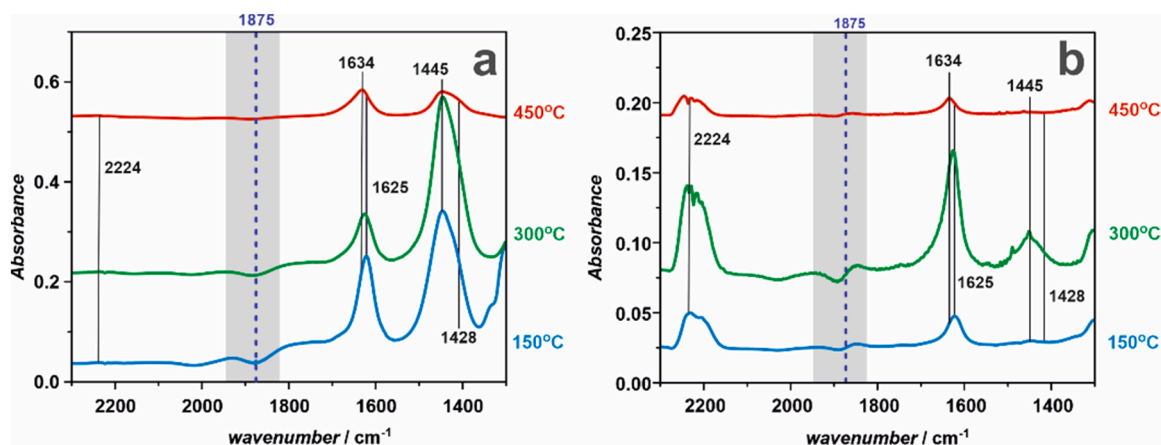


Fig. 6. IR spectra recorded at room temperature after the interaction of the samples of o-CuSSZ-13 (a) and i-CuSSZ-13 (b) with the stoichiometric SCR mixture ($\text{NH}_3 + \text{NO} + \text{O}_2$) at milestone temperatures (150 °C, 300 °C and 450 °C).

intensity at ~ 300 °C. Such bands have negligible intensity in the o-CuSSZ-13 sample, despite higher abundance of the Brønsted acid sites (NO^+ can be produced on BAS from a NO/O_2 mixture with production of water [64]). This observation points to other pathway of NO^+ formation that is in closer relation to the SCR mechanism [65]. Another noteworthy feature of both IR spectra is a distinctly different evolution of the bands 1625 cm^{-1} and $1440\text{--}1450\text{ cm}^{-1}$ with the increasing temperature (Fig. 6). Upon passing from 150 °C to 300 °C, the band at 1625 cm^{-1} for o-CuSSZ-13 decreases, whereas in the case of i-CuSSZ-13 its intensity increases, despite ammonia desorption. The shift in position and the shape changes of both bands once the temperature has reached 450 °C are also well pronounced, and in part caused by H_2O formation (the peak at 1634 cm^{-1}). These observations definitely confirm the complex nature of these bands, recognized earlier in the NH_3 oxidation experiments (see Fig. S12). For a more detailed insight into the relevance, dynamics, and reactivity of the key species that contribute to evolution of the $1621\text{--}1634\text{ cm}^{-1}$ and $1440\text{--}1450\text{ cm}^{-1}$ bands during the SCR reaction, time-resolved IR spectra were acquired in the Rapid Scan mode. The corresponding 2D COS maps, where three distinguished stages of the SCR reaction are well manifested, are shown in Fig. 7.

The first map, acquired at 150 °C (Fig. 7a), shows an initial stage of

the SCR process. Almost all correlations are positive, which can be explained in terms of the accumulation of surface intermediates, characterized by the bands located at 1634 , 1625 , 1590 , 1428 and 1370 cm^{-1} , which are merely perceivable in the standard IR spectra (Fig. 6). The most reactive intermediate under these conditions is Cu-NH_3 (1625 cm^{-1}), whose dynamics is correlated with bands at 1428 cm^{-1} (proximal NH_4^+ , $\text{O}=\text{N-NH}_2$) and 1370 cm^{-1} ($-\text{NH}_2$ [33] and free NO_3^- species [66]). As can be inferred from the changes in the autocorrelation peak of Cu-NH_3 , yet its behavior is also influenced by the dynamics of ammonia sorption. This is confirmed by the positive correlation between the gas phase NH_3 ($1865\text{--}1705\text{ cm}^{-1}$) and the $\text{Cu}^{2+}\text{-NH}_3$ adduct (1625 cm^{-1}) (not shown). The lack of an apparent correlation of the distal NH_4^+ band (1445 cm^{-1}) with any other detected species implies that at this temperature its concentration is maintained at virtually the same level. This provides a direct evidence that distal NH_4^+ are acting as spectators only. It confirms nicely the previous SCR mechanistic proposals, which have shown the independence of the SCR rate on the number of distal BAS sites left upon copper exchange [67, 68]. The weak negative correlations ($1625\text{ cm}^{-1} \times 1310\text{ cm}^{-1}$) and ($1625\text{ cm}^{-1} \times 1490\text{ cm}^{-1}$) reflect the initialization of the SCR process by the consumption of Cu -bonded NH_3 molecules with the parallel

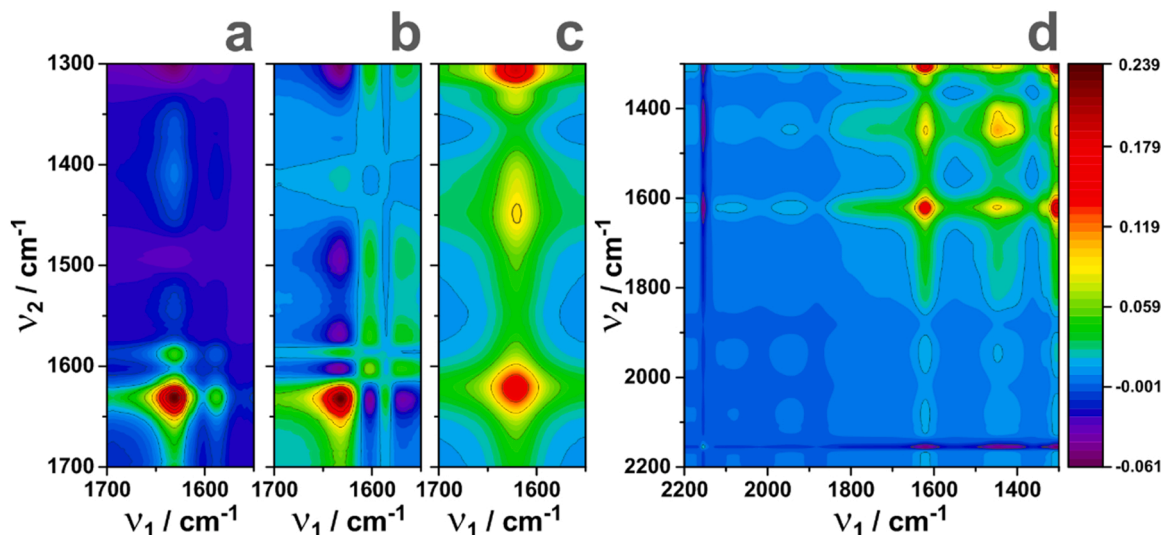


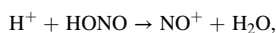
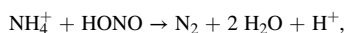
Fig. 7. Representative 2D correlation maps of IR frequencies in the range of NO_x and ammonia vibrations recorded in the Rapid Scan mode (scan took up to 2 min; one IR spectrum is an average of 5 scans recorded for 0.32 s in total) for o-CuSSZ-13 at 150 °C (a), 300 °C (b), and 400 °C (c), together with an expanded to higher frequencies 2D spectrum recorded at 400 °C (d). Because of recording of the 2D spectra at increasing temperatures, the band positions are shifted to lower frequencies, and in the text we use the band frequencies from the spectra recorded at room temperature, to avoid confusion.

formation of $\text{NO}_3^-/\text{NO}_2^-$ ($1310, 1490\text{ cm}^{-1}$).

At $300\text{ }^\circ\text{C}$ (Fig. 7b), new and strong correlations involve the 1590 and 1570 cm^{-1} bands due to bidentate and monodentate nitrates, all coupled to the 1625 cm^{-1} band of the copper ammonia adduct. They exhibit a negative sign, indicating extensive depletion of the corresponding nitrate and ammonia complexes, which interacting mutually drive the SCR process. These nitrate bands are completely obscured in the normal IR spectra when NO , NH_3 , and O_2 are co-adsorbed simultaneously (Fig. 6), but are clearly resolved as the cross-correlation peaks in the 2D COS maps. The nitrates with the 1590 and 1570 cm^{-1} peaks are seen upon coadsorption of NO and O_2 (Fig. S14a). This observation implies that the actual concentration of nitrates at the highest NO conversion rate becomes rather small, in agreement with the isotopic results (Fig. 5).

In this region, the number of proximal NH_4^+ species remains at a nearly constant level, as implied by the weak cross-correlation peak. Noting the high sensitivity of the 2D IR COS technique to even small changes in intensity, it indicates that the proximal NH_4^+ generated in the RHC step is next congruently consumed by interacting with nitrates, which is required for rapid SCR turnovers, accounting for the high conversion observed in this temperature region.

At $400\text{ }^\circ\text{C}$, the correlation ($1625\text{ cm}^{-1} \times 1310\text{ cm}^{-1}$) becomes strongly positive. Furthermore, a new positive correlation develops between the 1445 cm^{-1} band (distal NH_4^+) and the 1630 cm^{-1} band (NO_3^-). The correlation sign (supported by the inspection of the 1D spectra, Fig. 6) points to their simultaneous disappearance. The map plotted in the wider frequency range (Fig. 7d) additionally shows the presence of NO^+ adspecies (2160 cm^{-1}), strongly and negatively correlated with the $1310, 1490, 1428$, and 1630 cm^{-1} bands. All these observations indicate that at $400\text{ }^\circ\text{C}$ distal NH_4^+ species (with ammonia held more strongly than in Cu-NH_3 adducts [49]), become reactive. Their pronounced negative correlation with NO^+ species can be explained in the following terms,



where NO^+ is produced at the expense of distal NH_4^+ species through the intermediacy of the itinerant HONO . The latter is produced by the NO interaction with $\text{Cu}^{2+}\text{-OH}^-$, which couples the remote copper and BAS centers. HONO triggers the reactivity of distal NH_4^+ that is acting as an ultimate reservoir of NH_3 , driving the SCR process at its terminal stage (t-SCR). The NO^+ species, in turn, can also react with NH_3 , producing N_2 [65]:



Previous studies indicate that only the barrier for HONO interaction with NH_4^+ is considerable (1.08 eV), while for the other processes the barriers are rather small [65].

The described pathways are more productive at high temperatures than those based on Cu-NH_3 and nitrate intermediates, as the latter become nearly drained in the high temperature range of SCR (Figs. 6,7 and Fig. S14).

In supplementary experiments, the reactivity of various NO_3^- species with NH_3 (revealed by the cross-peaks in Fig. 7) was assessed by IR at 2D COS measurements (see Fig. S14a,b, and the corresponding discussion in Section 6 in Supporting Information). Briefly, the monodentate nitrates (1505 cm^{-1}) decay first, partly because they are less strongly bound. The bidentate nitrates characterized by the 1590 and 1570 cm^{-1} bands are more reactive than those with 1626 cm^{-1} . The characteristic peaks at 1445 and 1428 cm^{-1} of the distal and proximal NH_4^+ species produced upon NH_3 adsorption and SCR reaction, respectively, are also clearly developed. Their consumption above $350\text{ }^\circ\text{C}$ is well confirmed.

3.5. DFT and FPT modeling results

To substantiate the interpretation of the obtained results and advance the mechanistic considerations, the experimental investigations were corroborated by complementary DFT and ab initio thermodynamic modeling of the selected critical molecular events of the SCR/AMO reactions.

3.5.1. Reactant capture and N-H bond activation routes

The inherent redox character of the SCR and AMO reactions implies the existence of copper species in the cycling oxidized and reduced forms [8,13,26]. The oxidation state of copper dramatically changes its ability to capture the NH_3 , NO and O_2 reactants [8,10,22,37,49]. To map the stability regions of the copper adducts that are relevant for the SCR and AMO reactions, we constructed 2D thermodynamic diagrams for the selected copper centers in the oxidized and reduced states, setting $p_{\text{NO}} = p_{\text{NH}_3}$ and $p_{\text{O}_2} = 4.5 \times 10^{-2}$, $p_{\text{H}_2\text{O}} = 3.0 \times 10^{-2}$, according to the experimental conditions of the $\text{NO}:\text{NH}_3 = 1:1$ stoichiometry. This approach allows for modeling the formation of various mixed ligand species under given conditions, and comprehensive presentation of the results in a single 2D diagram (Fig. 8).

It is apparent from Fig. 8a that divalent copper forms only ammonia adducts of a gradually decreasing number of the NH_3 ligands with increasing temperature, as reported earlier [37,49,69]. However, in the case of $\tau\text{-Cu}^{2+}$ centers, the formation of mixed $\text{Cu}^{2+}(\text{NH}_3)(\text{NO}_3)$ complexes together with $\text{Cu}^{2+}(\text{NH}_3)$ can also be expected under the SCR conditions (Fig. 8b). At low temperatures ($T < 200\text{ }^\circ\text{C}$), the appearance of NO_2 and N^{18}O , when $^{18}\text{O}_2$ is used as an oxidant (Fig. 3 and Fig. 4), confirms the formation of nitrates during the SCR reaction. Indeed, once Cu^{2+} is reduced in the RHC step (by NH_3 or HONO), the resulting Cu^+ cations are preferentially “scavenged” by nitrates (NO and O_2), and the coordination sphere of the oxidized copper cations is complemented by NH_3 (Fig. 8c,d). Facile nitrate formation occurs even at low temperatures, as documented by an auxiliary EPR experiment, where after the introduction of the NO and O_2 mixture into the pre-reduced CuSSZ-13 samples, the characteristic EPR signal of Cu^{2+} species with nitrate ligands was easily restored, in agreement with previous findings [21]. In the case of the $\sigma\text{-Cu}^{2+}$ centers, the mixed ligand complexes are expected to be stable up to $200\text{--}220\text{ }^\circ\text{C}$, turning next into bare nitrates (lasting up to $450\text{--}500\text{ }^\circ\text{C}$), while for the $\tau\text{-Cu}^{2+}$ centers, the mixed ligand adducts persist at much higher temperatures ($400\text{ }^\circ\text{C}$), coexisting with the copper nitrates (dotted lines) and $\text{Cu}^+\text{-NH}_3$ species (Fig. 8c,d). As a result, the coordination environment of copper is intrinsically controlled by its oxidation state, which continuously cycles in the course of the SCR and AMO reactions.

The constructed 2D FPT diagrams for the Cu^{2+} and Cu^+ centers provide a useful thermodynamic support for the interpretation of the catalytic (isotopic) and IR results, as well as for the mechanistic considerations of the SCR/AMO reactions. An important implication of the obtained results is that the nature of the primary reaction intermediates may vary with the temperature, from ammino to mixed ligand and nitrate cage complexes, which can coexist in the temperature window of the highest SCR activity. Definitely, the catalytic reactivity of the copper centers is expected to cease above $450\text{--}500\text{ }^\circ\text{C}$ due to the loss of the reactive ligands (NH_3 and NO_3^-) captured by both Cu^{2+} and Cu^+ centers, see Fig. 8a-d). The mixed aqua-ammonia complexes (with $\tau\text{-Cu}$ sites) are stable only beyond the onset of the SCR reaction, and therefore, are not relevant directly.

The dual $\text{Cu}^{2+}\text{-O-Cu}^{2+}$ centers are characterized by the presence of a bridging oxygen of unique reactivity, which is capable of NO oxidation and activation of the reluctant N-H bonds of ammonia. The thermodynamic stability of various adspecies formed at the $\text{Cu}^{2+}\text{-O-Cu}^{2+}$ sites as a function of temperature is illustrated in Fig. 9. Two interesting features worth highlighting are the domination of nitrates and nitrites below $200\text{ }^\circ\text{C}$ ($\text{Cu}^{2+}\text{-O-Cu}^{2+} + 2\text{NO} + \text{O}_2 \rightarrow \text{Cu}^{2+}\text{-NO}_2 + \text{Cu}^{2+}\text{-NO}_3$), and the dissociative insertion of NH_3 into the metal-oxo bond ($\text{Cu}^{2+}\text{-O-Cu}^{2+} +$

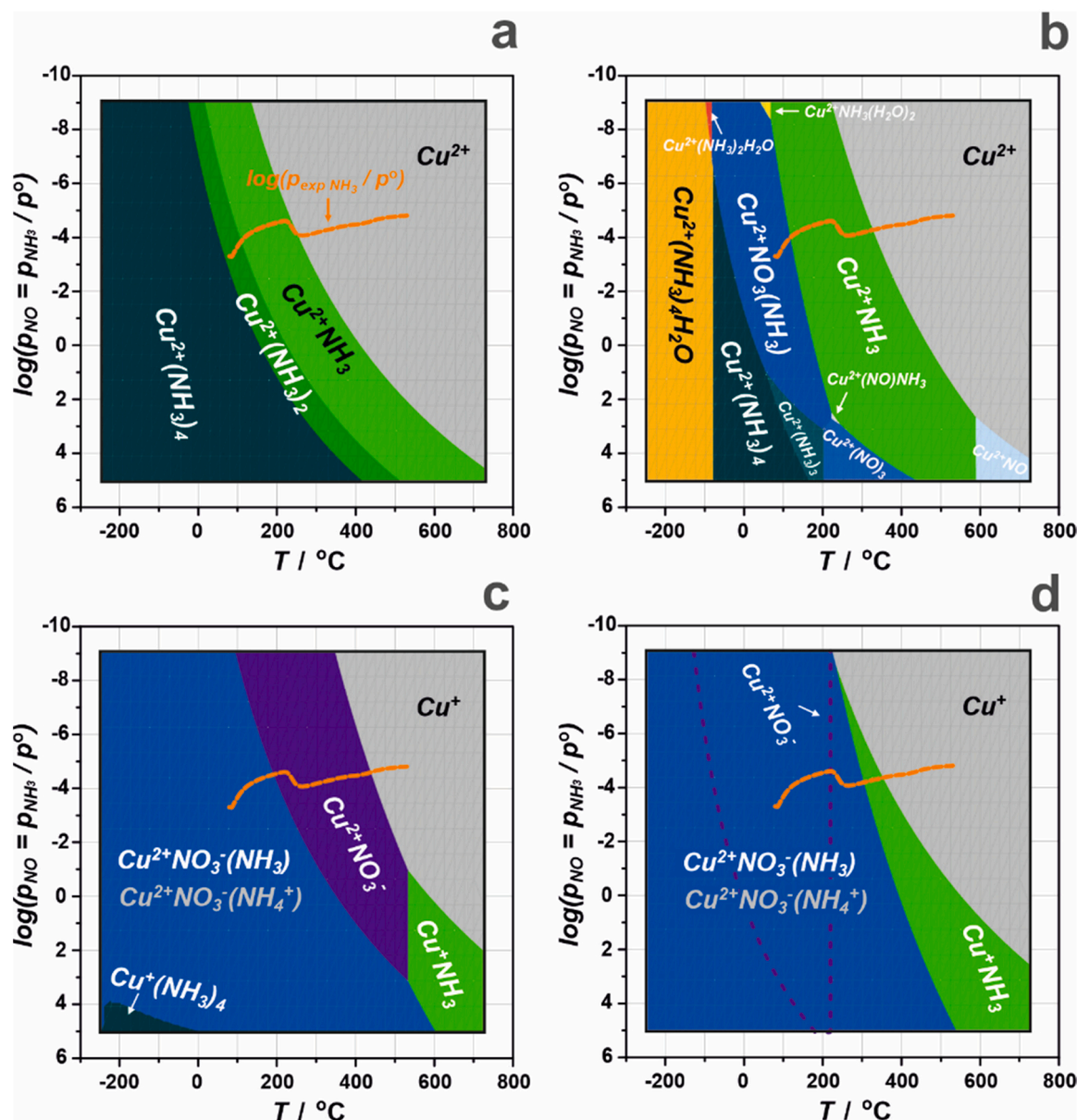


Fig. 8. Ab initio thermodynamic modeling of the capture and accommodation of SCR reactants over σ - Cu^{2+} (a, c) and τ - Cu^{2+} (b, d) centers for $p(\text{NO}) = p(\text{NH}_3)$, $p(\text{O}_2) = 4.5\%$, $p_{\text{H}_2\text{O}} = 3\%$. The dotted orange line shows the experimental variation in the partial pressure of NH_3 during the SCR reaction (above 150°C).

$\text{NH}_3 \rightarrow \text{Cu}^{2+}\text{-OH}^- + \text{Cu}^{2+}\text{-NH}_2$). The threshold temperature of the latter (200°C) coincides nicely with the onset of the NH_3 oxidation reaction (see Fig. 5).

All these findings provide the necessary thermodynamic rationale for the participation of $\text{Cu}^{2+}\text{-O-Cu}^{2+}$ centers in the facile dissociation of NH_3 , which in the temperature range of $200 - 300^\circ\text{C}$ is a prevalent process. Participation of $\text{Cu}^{2+}\text{-OH}^-$ in such reaction, though feasible (see the IR spectra shown in Fig. S12), is hampered by the competitive interaction with NO, which leads with low activation energy (0.25 eV) to the formation of a HONO molecule (Fig. S16), the secondary key intermediate of the SCR reaction [70,71].

The growth of the IR peak of NH_4^+ (1445 cm^{-1}) during the AMO and SCR reactions implies the operation of an electroprotic mechanism of the reductive interaction of NH_3 with the isolated Cu^{2+} sites ($\text{Cu}^{2+} + 2\text{NH}_3 \rightarrow \text{Cu}^+\text{-NH}_2 + \text{NH}_4^+$), where the proton released during the scission of the N-H bond is stabilized as NH_4^+ in the chabazite cage (see the IR results). It can be regarded as an outer-sphere ligand-to-ligand proton transfer, because without the assistance of an auxiliary ammonia

molecule this reaction is thermodynamically strongly disfavored (by 1.5 eV). The energetic profiles of the N-H bond splitting pathways are shown in Fig. 10. In particular, the NH_4^+ species can also be produced with the help of a NO molecule ($\text{NH}_3\text{-Cu}^{2+} + \text{NO} + \text{NH}_3 \rightarrow \text{Cu}^+\text{-ONNH}_2 + \text{NH}_4^+$) with a barrier of 0.74 eV [37]. However, since the resulting H_2NNO species is formed with the involvement of NO, it cannot be considered a common intermediate for the SCR and AMO reactions, in contrast to -NH_2 .

Dissociation of NH_3 on the $\text{Cu}^{2+}\text{-O-Cu}^{2+}$ centers is the most favorable event, both from the thermodynamic ($\Delta E_{\text{rdn}} = -0.68\text{ eV}$) and kinetic ($\Delta E_{\text{act}} = 0.71\text{ eV}$) viewpoints. In the temperature window of $200 - 300^\circ\text{C}$ it is apparently not much distracted by other competitive processes (see Fig. 9). For the $\text{NH}_3\text{-Cu}^{2+}\text{-OH}^-$ centers, the barrier of the inner sphere ligand-to-ligand proton transfer between the -OH^- and -NH_3 ligands is apparently the highest ($\Delta E_{\text{act}} = 1.32\text{ eV}$), and thermodynamically almost neutral. However, this pathway of ammonia activation is feasible only during the AMO reaction, as under SCR conditions (presence of NO) it is circumvented by much easier formation of the

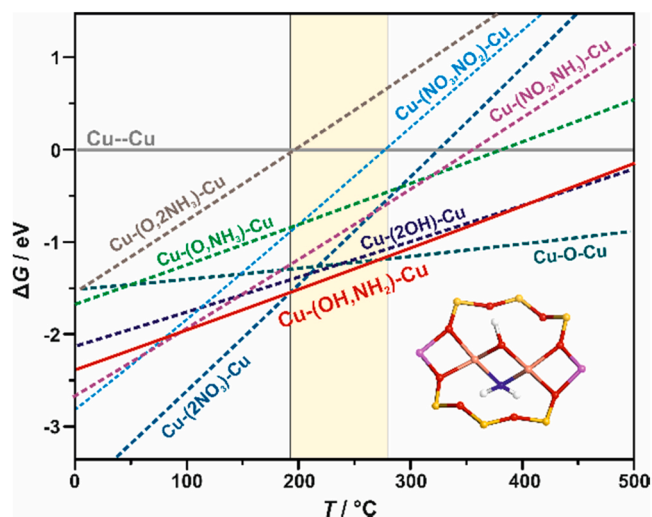


Fig. 9. Thermodynamic phase diagram for the interaction of the $\text{Cu}^{2+}\text{-O-Cu}^{2+}$ centers with the SCR reactants ($p_{\text{NH}_3} = 10^{-5}$ atm, $p_{\text{NO}} = 10^{-5}$ atm, $p_{\text{H}_2\text{O}} = 3 \cdot 10^{-2}$ atm, $p_{\text{H}_2\text{O}} = 4 \cdot 10^{-2}$ atm). The yellow stripe indicates the region where dissociative adsorption of NH_3 dominates, and the structure of the resultant species is shown in the right corner.

HONO intermediate ($\text{Cu}^{2+}\text{-OH}^- + \text{NO} \rightarrow \text{Cu}^+ + \text{HONO}$) with ΔE_{act} of 0.25 eV only (Fig. S16).

For the outer sphere mechanism operating in the case of the Cu^{2+} sites, the N-H splitting barrier drops to 1.01 eV, yet this reaction step is of a slightly uphill character (Fig. 10c₁-c₃). Nevertheless, it may thermodynamically be driven by the next step of the -NH_2 oxidation that leads to the formation of NO and N_2 upon the competitive reactions with O_2 or NO, respectively. The corresponding energy profiles for the Cu^{2+} and $\text{Cu}^{2+}\text{-O-Cu}^{2+}$ centers are shown in Figs. 11 and 12).

Oxidation of the -NH_2 moiety into NO by O_2 is thermodynamically allowed and kinetically not impeded ($\Delta E_{\text{act}} = 1.08$ and 1.13 eV for Cu^{2+} and $\text{Cu}^{2+}\text{-O-Cu}^{2+}$, respectively, Fig. 11a₁-a₄, and Fig. 11b₁-b₄), but must compete with the more favorable SCR reaction with gaseous NO ($\Delta E_{\text{act}} = 0.898$ eV and 0.76 eV), leading to the desired formation of N_2 (Fig. 12a₁-a₆ and Fig. 12b₁-b₆). An imide pathway of the NH_3 oxidation, triggered by the release of the second proton, is energetically strongly disfavored for both Cu^{2+} (Fig. S17a₁-a₃) and $\text{Cu}^{2+}\text{-O-Cu}^{2+}$ centers (Fig. S17b₁-b₃).

The mechanism of an external NH_3 (e-AMO) and NO oxidation on the segregated CuO nanoparticles is discussed in detail in Section 8, **Oxidation of NH_3 and NO on CuO nanoparticles – DFT and FPT modeling** (Supporting Information). The results imply that the reaction is controlled by formation of transient surface peroxo O_2^- intermediates and oxygen vacancies, which are primarily responsible for both oxidation processes occurring concurrently. The proposed elementary steps and the energetic landscapes of those reactions were calculated, and the predicted profiles of the O_2 and NO_2/NO release from the surface of the CuO nanocrystals remain in remarkable agreement with the experimental ones (Fig. S19d, compare blue and dotted gray lines). This allows for straightforward interpretation of the mechanistic origin of three types of the exhaust NO molecules: the intact (ex-feed $^{14}\text{N}^{16}\text{O}$) and the altered NO (ex-nitrates $^{14}\text{N}^{18}\text{O}$ and ex-ammonia oxidation $^{15}\text{N}^{18}\text{O}/^{15}\text{N}^{16}\text{O}$), as well as for the extensive formation of $^{16}\text{O}^{18}\text{O}$ (Fig. 4). The mechanism with the corresponding energetics of NH_3 oxidation into NO along alternative imide (-NH) and amide (-NH_2) pathways is shown in Fig. S21. In the imide route formation of the N-O bond occurs via an H-N=O intermediate, whereas the amid one via an H-O=NH intermediate.

4. Discussion

The described isotopic and spectroscopic studies of the NH_3 -SCR process, complemented by DFT/FPT modeling, provided a crucial

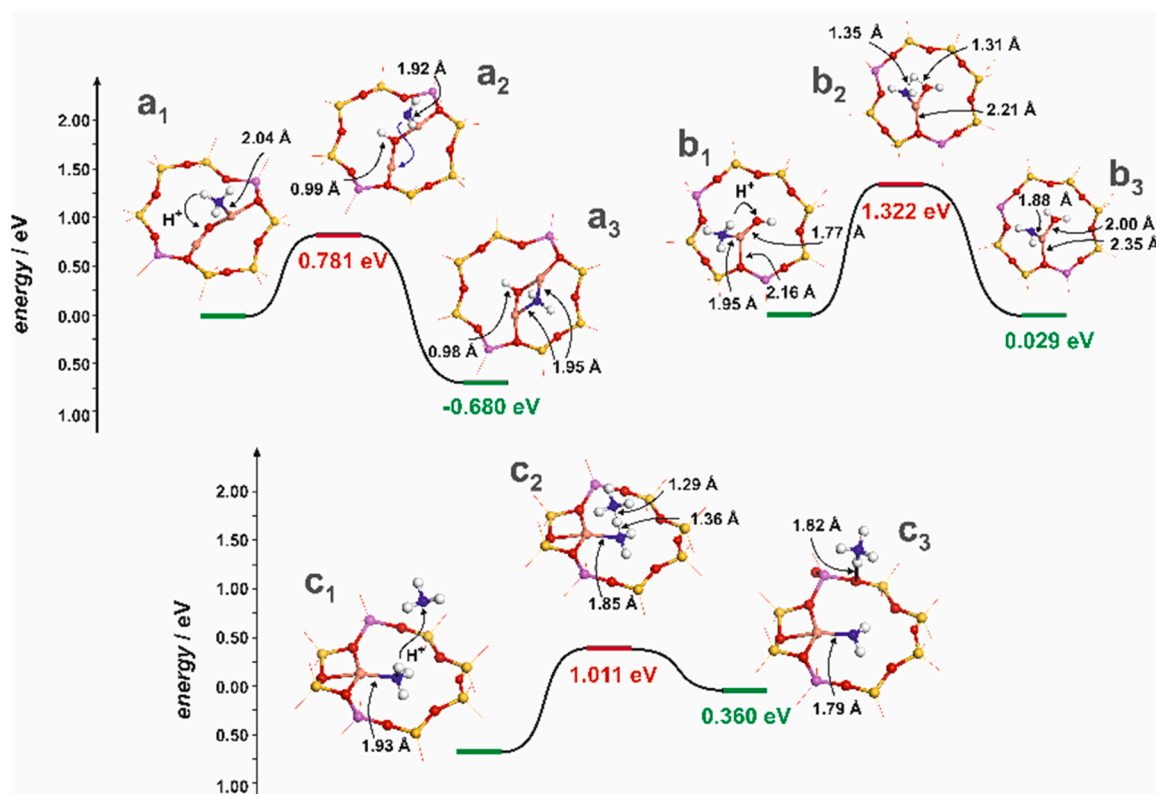


Fig. 10. Energetic profiles of the N-H bond splitting steps of the NH_3 activation over the $\text{Cu}^{2+}\text{-O-Cu}^{2+}$ (a₁ - a₃), $\text{Cu}^{2+}\text{-OH}^-$ (b₁ - b₃), and Cu^{2+} centers (c₁ - c₃).

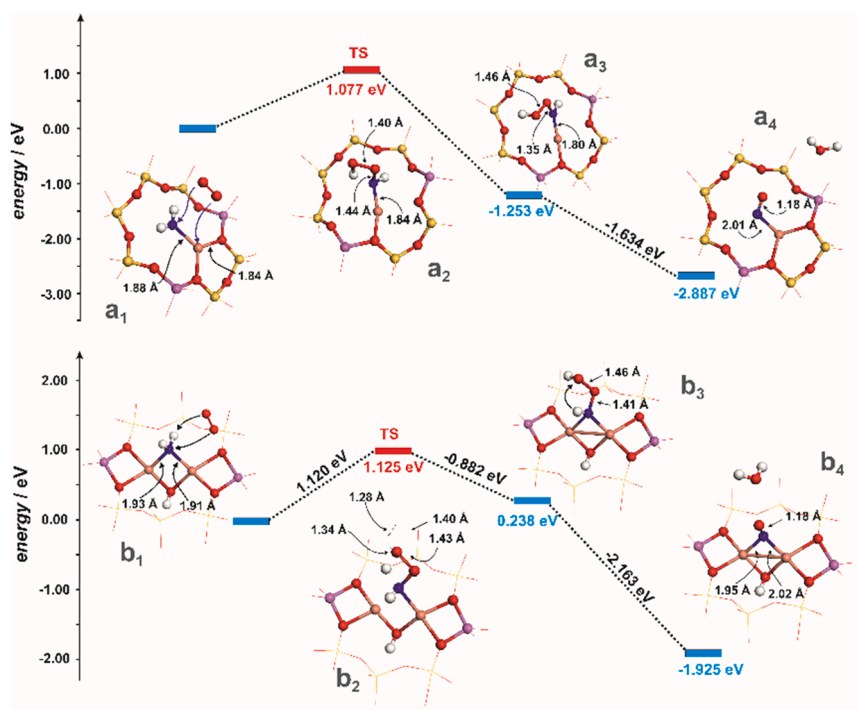


Fig. 11. Energy profile for oxidation of -NH_2 species over Cu^{2+} ($\text{a}_1\text{-a}_4$) and $\text{Cu}^{2+}\text{-O-Cu}^{2+}$ centers ($\text{b}_1\text{-b}_4$).

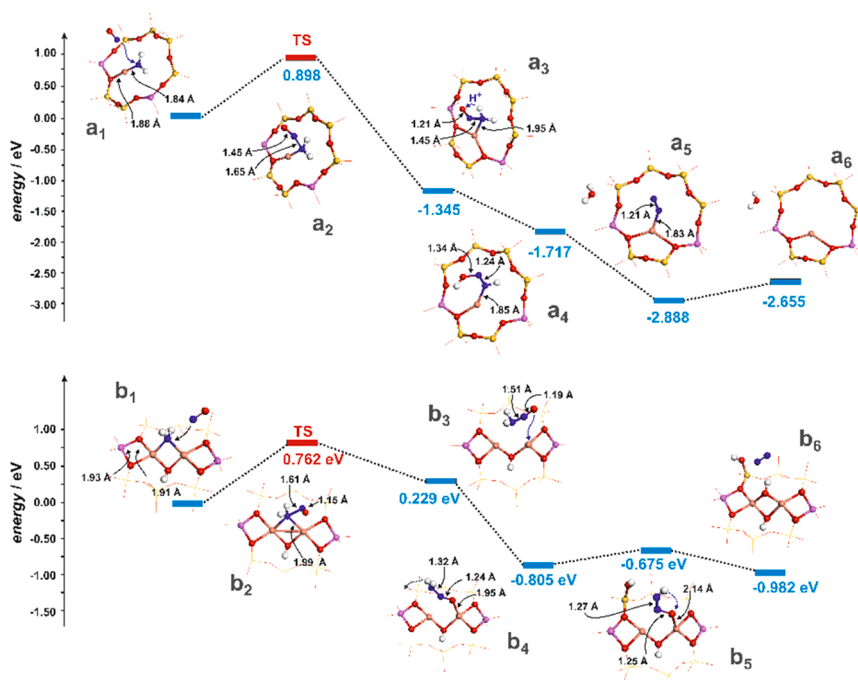


Fig. 12. Energy profile for NO interaction with -NH_2 species leading to N_2 formation over Cu^{2+} ($\text{a}_1\text{-a}_6$) and $\text{Cu}^{2+}\text{-O-Cu}^{2+}$ centers ($\text{b}_1\text{-b}_6$).

insight into the variety of interlacing reaction pathways, and the versatile character of the active sites and the key intermediates, whose mechanistic role changes with the reaction temperature. The primary finding of the catalytic investigations using the N-15 labeling is the lack of full congruence between the NO conversion and N_2 production. It results from the fact that part of N_2 comes from the concomitant oxidation of NH_3 into N_2 , which is favored when temporarily $p_{\text{NH}_3} > p_{\text{NO}}$. Another interesting feature revealed by the simultaneous presence of $^{14}\text{N}^{16}\text{O}$, $^{15}\text{N}^{16}\text{O}$, $^{14}\text{N}^{18}\text{O}$, and $^{15}\text{N}^{18}\text{O}$ in the reaction products,

when $^{15}\text{NH}_3$ and $^{18}\text{O}_2$ were used as reactants, is the development of NO in the high temperature region along three independent pathways. In addition to the external oxidation of ammonia to nitric oxide (e-AMO) over the segregated CuO nanoparticles (^{15}NO , $^{15}\text{N}^{18}\text{O}$), contributions of nitric oxide implicated in the intrazeolite nitrate/nitrite cycle (N^{18}O), and from intact NO (passing through the catalyst bed) have been identified in the NO outflow.

The maxima in the N_2 profile observed in the temperature-programmed SCR experiments are caused by the temporal selectivity

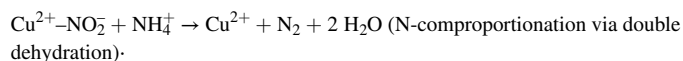
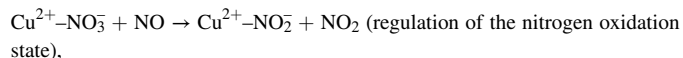
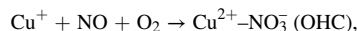
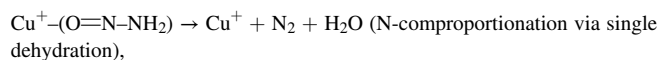
drop, due to the release of NH_3 from the coordination sphere of the copper adducts, which accelerates the internal oxidation of ammonia. This leads to a significant disparity of the N_2 formation in the concurrent SCR and i-AMO reactions, in the temperature range of 280–360 °C (Fig. 13a) where the NH_3 molecules are released (see Fig. 13b, solid purple line). The DFT calculated profile (Fig. 13b, dotted green line) of the molecular NH_3 desorption from $\text{Cu}^{2+}\text{--O}^{2-}\text{--Cu}^{2+}$ shows that such centers should then be bare and ready for dissociative accommodation of the cage NH_3 molecules, which triggers their subsequent oxidation.

Furthermore, inspection of Fig. 13c shows a pronounced lack of N_2 production parity in the i-AMO (i-SCR) reaction and in a separate AMO ($\text{NH}_3\text{--SCO}$) experiment. As a result, the latter activity cannot be directly used for interpretation of the selectivity loss in SCR over the same catalysts, even when both tests were performed at exactly the same conditions.

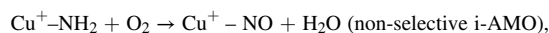
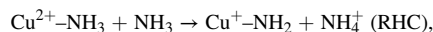
The obtained isotopic and spectroscopic results allowed us to distinguish 3 main SCR reaction regions (Fig. 14a). They are also well supported by the three clearly distinct reactivity patterns seen in the 2D COS maps (Fig. 7). The low temperature region (green area) features an incongruent adsorption/desorption dynamics of NO and NH_3 , leading to pronounced ammonia storage and significant temporal imbalance of the in-cage NH_3 to NO stoichiometry. This is essentially caused by the much higher capacity of Cu^{2+} to capture the NH_3 than NO molecules. Due to the excess of ammonia, it is called here an NH_3 -rich region. The initial stage of the sorption dynamics gradually evolves into the standard SCR reaction (s-SCR), which is essentially prevalent until 200 °C, and is characterized by even consumption of NH_3 and NO (1:1), despite the ammonia excess (stored in the zeolite). In this region, copper cations are solvated, which renders the s-SCR reaction to occur inside the zeolite cages, following the well-established mechanism, split into the RHC and OHC steps [2,6,8]. In this temperature window, nitrates can also be produced independently of the RHC/OHC sequence on the $\text{Cu}^{2+}\text{--OH}^-$ and $\text{Cu}^{2+}\text{--O}^{2-}\text{--Cu}^{2+}$ centers, without previous copper reduction by NH_3 (Fig. 14a).

In the temperature range of 200–400 °C (the second stage of SCR, yellow stripe in Fig. 14a), the conversion approaches maximum, and the partial pressure of ammonia drops drastically creating the NH_3 -lean conditions. The SCR reaction is now accompanied by the side ammonia oxidation (i-AMO), which proceeds essentially through the internal SCR mechanism. Furthermore, due to the autogenous NO_2 formation, the s-SCR and fast SCR (f-SCR) reactions can now occur simultaneously, and NO_2 is consumed accordingly (compare the solid and dotted blue lines in Fig. 14a, which indicate NO_2 production in the absence of NH_3 , and its uptake when NH_3 is present). These reactions are sustainably turned over the Cu^{2+} , $\text{Cu}^{2+}\text{--OH}^-$ and $\text{Cu}^{2+}\text{--O}^{2-}\text{--Cu}^{2+}$ centers, while the distal BAS centers behave as spectator species at this stage. The isolated Cu^{2+} sites are responsible for an electroprotic (electron transfer to Cu^{2+} and

proton transfer to proximal BAS) pathway of the N–H bond activation, $\text{Cu}^{2+}\text{--NH}_3 + \text{NO} + \text{NH}_3 \rightarrow \text{Cu}^+\text{--(O=N--NH}_2\text{)} + \text{NH}_4^+$. It is characterized by the formation of proximal NH_4^+ species and the $\text{H}_2\text{N}_2\text{O}$ intermediates of the favorable 2:2:1 stoichiometry, which is commensurate with the desirable N_2 and H_2O end products. Depending on the temperature, it occurs with the help of gas phase NO (particularly at low temperatures) and NH_3 molecules ($T > 200$ °C). Thus, the subsequent steps leading to N_2 formation, via comproportionation of the oppositely charged N atoms in the O=N- and -NH_2 moieties, can be formulated as:

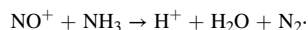
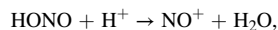
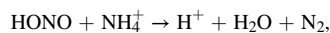


For the NH_3 oxidation, the reactions steps are:



Obviously, the Cu^+ cations are readily oxidized to $\text{Cu}^{2+}\text{--NO}_3^-$ in the presence of O_2 and NO.

The $\text{Cu}^{2+}\text{--OH}^-$ centers may act more versatily, giving rise to the formation of HONO – a stoichiometrically incommensurate (1:1:2) intermediate ($\text{Cu}^{2+}\text{--OH}^- + \text{NO} \rightarrow \text{Cu}^+ + \text{HONO}$) or the stoichiometrically commensurate (2:2:1) nitrosamine ($\text{Cu}^{2+}\text{--OH}^- + \text{NH}_3 + \text{NO} \rightarrow \text{Cu}^+\text{--(O=N--NH}_2\text{)} + \text{H}_2\text{O}$). The HONO route leads to copper reduction, without participation of NH_3 , which explains, *i.e.*, the appearance of nitrates upon interaction of the oxidized CuSSZ-13 samples with a mixture of NO and O_2 , and during the low temperature stage of SCR, as well. The HONO species also play an important role in the terminal stage of the reaction (t-SCR). Being mobile, they can react with the distal BAS, which act as important ultimate ammonia storage centers:



As a result, $\text{Cu}^{2+}\text{--OH}^-$ sites can operate alone as a source of HONO and nitrate species (the first and second stages of SCR), or in conjunction

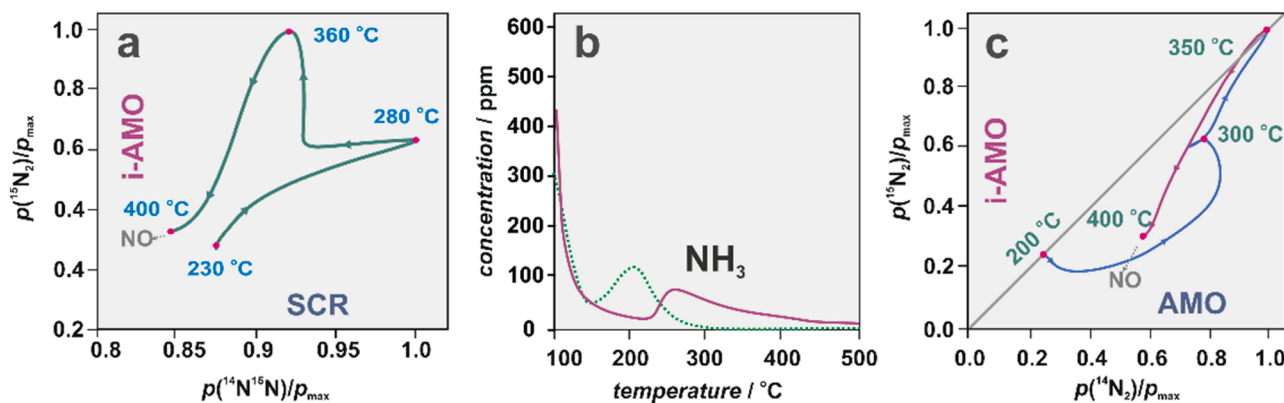


Fig. 13. Parity plots of N_2 formation in the course of concurrent reactions of reactions of SCR (NO reduction) and i-AMO (ammonia oxidation) (a), NH_3 desorption profile with the calculated release of ammonia from $\text{Cu}^{2+}\text{--O}^{2-}\text{--Cu}^{2+}$ centers marked with a dotted line (b) and the parity plot for the reactions of i-AMO and AMO (c), conducted under the same conditions.

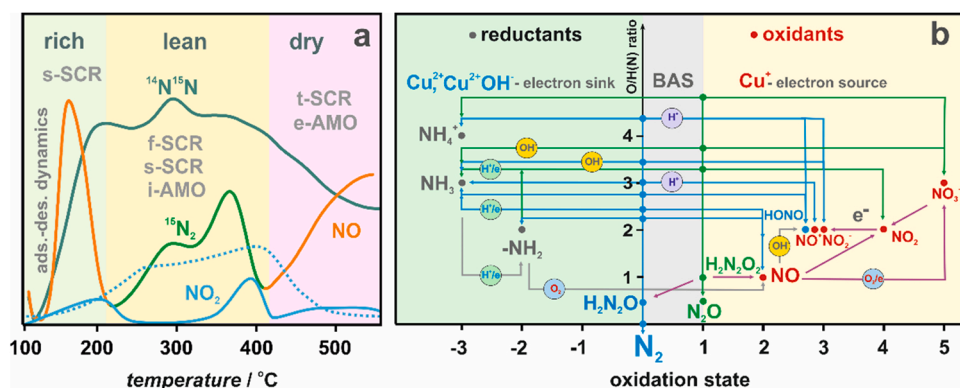


Fig. 14. Mechanistic stages of the SCR/AMO reactions over CuSSZ-13 catalysts (a) and the 2D commensurability diagram illustrating the stoichiometry, charge, and oxidation state constraints for the SCR/AMO reactants and intermediates (b). The species shown in the circles define the requisite pathways of compatibility regularization. Blue lines connect the commensurate intermediates leading to N_2 , green lines connect incommensurate species leading to N_2O , whereas the purple lines refer to regulation of the nitrogen oxidation state in the $\text{NO}/\text{NO}_2/\text{NO}_2^-/\text{NO}_3^-$ sub-cycle.

with distal BAS centers through space, by taking advantage of the itinerant character of HONO (late stage of the reaction). This explains the formation of NO^+ in the case of o-CuSSZ-13 with the high concentration of $\text{Cu}^{2+}\text{-OH}^-$, and the absence of NO^+ for i-CuSSZ-13, where the $\text{Cu}^{2+}\text{-OH}^-$ centers are much less abundant, as well as the revealed 2D COS correlation between NO^+ and NH_4^+ (Fig. 7). In contrast, the Cu^{2+} centers can jointly act with the proximal BAS only. Upon the RHC step, the original state of such tandem active site is restored most readily via an electroprotic interaction of the resultant Cu^+/H^+ pair with NO_2 and NH_3 , respectively, leading to N_2 formation after double dehydration of NH_4NO_2 (f-SCR).

The formation of nitrates already in the first stage of the reaction, in addition to the HONO route, can be formulated as $\text{Cu}^{2+}\text{-O}^{2-}\text{-Cu}^{2+} + \text{O}_2 + 2\text{NO} \rightarrow \text{Cu}^{2+}\text{-NO}_3^- + \text{Cu}^{2+}\text{-NO}_2^-$ [19], accounting for the isotopic exchange between NO and $^{18}\text{O}_2$ and NO_2 evolution during SCR. A facile generation of nitrates confirms that the classic sequence of the SCR steps (copper reduction by the NO/NH_3 mixture and reoxidation by NO/O_2) can partly be reversed, as mentioned above. As the bidentate copper nitrates are more stable than ammonia complexes (Figs. 8 and 9), such reversal gains in importance in the second and third stages of the reaction.

In the NH_3 -lean stage of the SCR reaction (Fig. 14a, yellow area), the dual copper-oxo sites become additional centers for NH_3 dissociation ($\text{Cu}^{2+}\text{-O}^{2-}\text{-Cu}^{2+} + \text{NH}_3 \rightarrow \text{Cu}^{2+}\text{-OH}^- + \text{Cu}^+\text{-NH}_2$). Subsequent oxidation of -NH_2 into NO/NO_3^- triggers the i-AMO reaction.

The terminal stage of the SCR reaction (t-SCR) begins at $T > 400^\circ\text{C}$ (Fig. 14a, pink area), and is characterized by a strong exhaustion of the copper-ammonia cage complexes (NH_3 dry conditions), rationalized by the FPT results (Fig. 8). It drives the SCR reaction toward the involvement of the thermally more stable distal NH_4^+ centers, and when segregated CuO is present to the development of a parallel e-AMO reaction, where O_2^{2-} and oxygen vacancies play the crucial mechanistic role (see the discussion in Section 8, Supporting Information).

For a straightforward conceptualization of the large variety of possible reactivity patterns that constitute the mechanistic network of the SCR/AMO reactions, we propose a 2D commensurability diagram where the NO/NH_3 reactants and the key intermediates are ordered, according to their oxidation state and the O/H(N) ratio (Fig. 14b). Such diagram reveals the principal stoichiometry, charge and oxidation state compatibility constraints between the reactants and the intermediates, revealing the primary modes of their regulation for a straightforward turnover of the SCR/AMO reactions. In this context, the essence of the SCR/AMO mechanisms consists in the comproportionation of the positively (NO) and negatively (NH_3) charged nitrogen atoms, which provides a prime molecular requisite for the facile formation of the N–N bond. It is intrinsically controlled by the disparity between the oxidation state of nitrogen in N^{2+}O and N^{3+}H_3 , and the stoichiometric imbalance between the N, H, and O atoms with respect to the commensurate 2:2:1 at. ratio, which is directly leading to the formation of N_2 and H_2O .

These mechanistic issues are cogently epitomized in the 2D commensurability diagram (Fig. 14b). On the left side (marked in green), the parent NH_3 and its activated derivatives NH_4^+ and -NH_2 (acting as reductants), while on the right side the oxidants NO , NO_2 , and $\text{NO}_2^-/\text{NO}_3^-$ are put together. All of these species were detected during the course of the reaction. The elusive HONO, $\text{H}_2\text{N}_2\text{O}$, and $\text{H}_2\text{N}_2\text{O}_2$ are difficult to be spectroscopically detected, (possibly with exception of $\text{H}_2\text{N}_2\text{O}$, 1428 cm^{-1}), yet their pivotal mechanistic role is well established by the DFT modeling [6,10,12,38]. The constructed 2D diagram of the prime reactivity patterns shows that regularization of the stoichiometry and the net charge between the reductant and the oxidant species can be achieved via the electroprotic pathway (H^+/e^-), where the Cu^{2+} (electron sink) and proximal BAS (proton sink) sites act together, or through the OH^- ligand ($\text{Cu}^{2+}\text{-OH}^-$ centers), which can be reductively eliminated and replaced by $\text{NO}_3^-/\text{NO}_2^-$ (to satisfy the charge balance constraint).

The blue lines connect those pairs of the reductant and oxidant intermediates, which directly, or upon simple regularization, are mutually commensurate with respect to their stoichiometry, net charge, and oxidation state, leading next to the desired N_2 as a final product. The necessary regularization between these species can be affected by the elementary OH^- , H^+ , H^+/e^- and O_2/e^- redox/acid-base interactions with the active sites.

The intermediates connected by green lines constitute the redox pairs of the stoichiometry or charge incompatibility that cannot be simply adjusted by the transfer of the OH^- , H^+/e^- or H^+ species, leading ultimately to the formation of N_2O . Stoichiometric regularization of nitrogen oxides and nitrates (purple lines) is carried out through the N-oxidation state sub-cycle ($\text{NO}_3^- + \text{NO} \rightarrow \text{NO}_2^- + \text{NO}_2$), whose efficiency is crucial for the SCR selectivity, and for dehydration of $\text{NH}_4^+\text{NO}_3^-$. In fact, the activation energy of dehydration is reduced from 1.41 eV to 1.08 eV after transformation of nitrates into nitrites due to the interaction with NO , but noteworthy, the barrier of the latter process is markedly lower (0.75 eV) [72]. These results provide a rationale for circumvention of the undesired dehydration of NH_4NO_3 into N_2O , instead of N_2 (produced upon dehydration of NH_4NO_2). The commensurate $\text{H}_2\text{N}_2\text{O}$ intermediates, which are formed in the latter case, are not only fully regulated, but the N–N bond is already created between the nitrogen atoms. These intermediates can be easily dehydrated into N_2 , in contrast to the overoxidized $\text{H}_2\text{N}_2\text{O}_2$ (derived from NH_4NO_3), which transforms into N_2O and H_2O .

The location of HONO in the proposed diagram (Fig. 14b) implies that, for its conversion into N_2 , it has to react with NH_3 or with NH_4^+ (with H^+ transfer the bare BAS center) to acquire the necessary 2:2:1 stoichiometry, as the oxidation states of these species are fully compatible (+3 and −3) for direct formation of the N–N bond. The role of HONO intermediates gains importance in the t-SCR stage, where distal NH_4^+ acts as a reservoir of adsorbed NH_3 . Owing to its volatile character, HONO can effectively react with residual ammonium cations

that are hardly accessible for the rigid copper nitrate/nitrite counterparts. As a result, $\text{Cu}^{2+}\text{-OH}^-$ and remote BAS begin to act cooperatively through space in the t-SCR stage via the itinerant HONO.

In summary, the proposed 2D commensurability diagram allows one to easily identify those reaction pathways that occur in a straightforward way or, impeded by the regularization of the H:O:N ratio, oxidation state or charge disparity, have to proceed in a more intricate fashion. Oxidation of Cu^+NO into $\text{Cu}^{2+}\text{NO}_3^-$ by O_2 (s-SCR) vs. Cu^+ by NO_2 into $\text{Cu}^{2+}\text{NO}_2^-$ (f-SCR) is decisive here, as it leads to the formation of over-oxidized $\text{H}_2\text{N}_2\text{O}_2$ (2:2:2) or stoichiometric $\text{H}_2\text{N}_2\text{O}$ (2:2:1) intermediates, respectively. To avoid unwanted N_2O formation, the overoxidation of the relevant intermediates is released by entering into the $\text{NO}/\text{NO}_2/\text{NO}_3^-$ sub-cycle. However, its complex anionic redox character (oxidation state of Cu^{2+} remains intact), renders the SCR reaction mechanistically sluggish. Depletion of the $\text{Cu}^{2+}\text{-NH}_3$ adducts indicates that NH_4^+ species, along with the remaining surface NO_3^- assume the role of the primary high-temperature intermediates of t-SCR, allowing for maintenance of the Eley-Rideal mechanism.

The observed in situ oxidation of excessive NH_3 (i-AMO) in the region of high conversion suggests benefits for the main SCR process from the adjustment of the ammonia dose at low temperatures, rather than continuously supplying NH_3 at a constant level [42]. This should not only limit the ammonia slip but also reduce its waste due to considerable unproductive oxidation (i-AMO).

5. Conclusions

The mechanism of the SCR and AMO reactions with the progression of temperature was revealed by isotopic TPSR and steady-state investigations using $^{15}\text{NH}_3$ and $^{18}\text{O}_2$ reactants, corroborated by IR/2D COS spectroscopic studies. Above $\sim 200^\circ\text{C}$, the SCR reaction is accompanied by ubiquitous internal NH_3 oxidation (i-AMO), which involves the $\text{Cu}^{2+}\text{-O}^{2-}\text{-Cu}^{2+}$ and Cu^{2+} centers. At $T > 400^\circ\text{C}$, when segregated CuO nanoparticles are present, an external oxidation of NH_3 (e-AMO) takes place, with O_2^- species as primary intermediates. The i-AMO reaction is triggered by a temporal excess of NH_3 with respect to NO , caused by the release of ammonia stored in the zeolite cages with the increasing temperature. Three temperature regions of the SCR/AMO reactions, corresponding to NH_3 -rich, lean, and dry conditions, were distinguished, and the main processes and intermediates of each stage were identified. For conceptualization of the SCR reaction mechanism, a 2D commensurability diagram was constructed. It reveals the principal stoichiometry (O/H(N) ratio), charge and N-oxidation state requirements between the reactants and intermediates, and prime modes of their regulation for straightforward turnover of the SCR/AMO reactions.

CRediT authorship contribution statement

Monika Fedyna: Investigation, Data curation. **Bartosz Mozgawa:** Investigation, Data curation, Visualization. **Filip Zasada:** Investigation, Data curation, Visualization. **Kinga Góra-Marek:** Investigation, Data curation, Validation. **Joanna Gryboś:** Investigation, Data curation. **Witold Piskorz:** Investigation, Software. **Chengyang Yin:** Investigation. **Zhen Zhao:** Writing – review & editing. **Piotr Pietrzyk:** Data curation, Validation, Writing – review & editing. **Zbigniew Sojka:** Methodology, Data curation, Validation, Writing – original draft, Writing – review & editing, Supervision, Funding acquisition.

Declaration of Competing Interest

The authors declare that they have no known competing financial interests or personal relationships that could have appeared to influence the work reported in this paper.

Data Availability

Data will be made available on request.

Acknowledgments

The work was carried out within the MOST program for collaboration between Poland and China, which is financially supported by The National Centre for Research and Development, Poland, grant PNOX No. WPC1/PNOX/2019, and from China side by the Project 2017YFE0131200. The Authors thank Dr. Janusz Janas for his help in performing catalytic test studies. The study was carried out using research infrastructure purchased with the funds of the European Union in the framework of the Smart Growth Operational Programme, Measure 4.2; Grant No. POIR.04.02.00-00-D001/20, “ATOMIN 2.0 - ATOMIC scale science for the INnovative economy”.

Appendix A. Supporting information

Supplementary data associated with this article can be found in the online version at doi:10.1016/j.apcatb.2022.122309.

References

- [1] Ch.K. Lambert, Perspective on SCR NOx control for diesel vehicles, *React. Chem. Eng.* 4 (2019) 969–974, <https://doi.org/10.1039/c8re00284c>.
- [2] A.M. Beale, F. Gao, I. Lezcano-Gonzalez, C.H.F. Peden, J. Szanyi, Recent advances in automotive catalysis for NO_x emission control by small-pore microporous materials, *Chem. Soc. Rev.* 44 (2015) 7371–7401, <https://doi.org/10.1039/c5cs00108k>.
- [3] D. Damma, P.R. Ettireddy, B.M. Reddy, P.G. Smirniotis, A Review of low temperature NH_3 -SCR for removal of NO_x , *Catalysts* 9 (2019) 349, <https://doi.org/10.3390/catal9040349>.
- [4] M. Jablonka, Progress on selective catalytic ammonia oxidation (NH_3 -SCO) over Cu-containing zeolite-based catalysts, *ChemCatChem* 12 (2020) 4490–4500, <https://doi.org/10.1002/cctc.202000649>.
- [5] H. Wang, R. Zhang, Y. Liu, P. Li, H. Chen, F.R. Wang, W.Y. Teoh, Selective catalytic oxidation of ammonia over nano Cu/zeolites with different topologies, *Environ. Sci.: Nano* 7 (2020) 1399, <https://doi.org/10.1039/D0EN00007H>.
- [6] C. Paolucci, J.R. Di Iorio, F.H. Ribeiro, R. Gounder, W.F. Schneider, Catalysis science of NO_x Selective Catalytic Reduction with ammonia over Cu-SSZ-13 and Cu-SAPO-34, *Adv. Catal.* 59 (2016) 1–107, <https://doi.org/10.1016/bs.acat.2016.10.002>.
- [7] E. Borfecchia, P. Beato, S. Svelle, U. Olsbye, C. Lamberti, S. Bordiga, Cu-CHA – a model system for applied selective redox catalysis, *Chem. Soc. Rev.* 47 (2018) 8097–8133, <https://doi.org/10.1039/C8CS00373D>.
- [8] F. Gao, Ch.H.F. Peden, Recent progress in atomic-level understanding of Cu/SSZ-13 selective catalytic reduction catalysts, *Catalysts* 8 (2018) 140, <https://doi.org/10.3390/catal8040140>.
- [9] M. Colombo, I. Nova, E. Tronconi, Detailed kinetic modeling of the NH_3 - NO/NO_2 SCR reactions over a commercial Cu-zeolite catalyst for Diesel exhausts after treatment, *Catal. Today* 197 (2012) 243–255, <https://doi.org/10.1016/j.cattod.2012.09.002>.
- [10] Ch. Paolucci, A.A. Verma, S.A. Bates, V.F. Kispersky, J.T. Miller, R. Gounder, W. N. Delgass, F.H. Ribeiro, W.F. Schneider, Isolation of the copper redox steps in the standard selective catalytic reduction on Cu-SSZ-13, *Angew. Chem. Int. Ed.* 53 (2014) 11828–11833, <https://doi.org/10.1002/anie.201407030>.
- [11] A.R. Fahami, T. Günter, D.E. Doronkin, M. Casapu, D. Zengel, T.H. Vuong, M. Simon, F. Breher, A.V. Kucherov, A. Brückner, J.-D. Grunwaldt, The dynamic nature of Cu sites in Cu-SSZ-13 and the origin of the seagull NO_x conversion profile during NH_3 -SCR, *React. Chem. Eng.* 4 (2019) 1000–1018, <https://doi.org/10.1039/c8re00290h>.
- [12] L. Chen, T.V.W. Jansen, P.N.R. Vennestrom, J. Jansson, M. Skoglundh, H. Gronbeck, A complete multisite reaction mechanism for low temperature NH_3 -SCR over Cu-CHA, *ACS Catal.* 10 (2020) 5646–5656, <https://doi.org/10.1021/acscatal.0c00440>.
- [13] M. Bendrich, A. Scheuer, R.E. Hayes, M. Votsmeier, Unified mechanistic model for standard SCR, fast SCR, and NO_2 SCR over a copper chabazite catalyst, *Appl. Catal. B: Environ.* 222 (2018) 76–87, <https://doi.org/10.1016/j.apcatb.2017.09.069>.
- [14] R. Villamaña, U. Iacobone, I. Nova, M.P. Ruggeri, J. Collier, D. Thompson, E. Tronconi, Low-T CO oxidation over Cu-CHA catalysts in presence of NH_3 : probing the mobility of Cu^{II} ions and the role of multinuclear Cu^{II} species, *ChemCatChem* 12 (2020) 3843–3848, <https://doi.org/10.1002/cctc.202000734>.
- [15] G. Yang, J. Ran, X. Du, X. Wang, Y. Chen, L. Zhang, Different copper species as active sites for NH_3 -SCR reaction over Cu-SAPO-34 catalyst and reaction pathways: a periodic DFT study, *Microporous Mesoporous Mater.* 266 (2018) 223–231, <https://doi.org/10.1016/j.micromeso.2018.01.034>.
- [16] E. Borfecchia, K.A. Lomachenko, F. Giordano, H. Falsig, P. Beato, A.V. Soldatov, S. Bordiga, C. Lamberti, Revisiting the nature of Cu sites in the activated Cu-SSZ-13

- catalyst for SCR reaction, *Chem. Sci.* 6 (2015) 548–563, <https://doi.org/10.1039/c4sc02907k>.
- [17] C. Fan, Z. Chen, L. Pang, S. Ming, X. Zhang, K.B. Albert, P. Liu, H. Chen, T. Li, The influence of Si/Al ratio on the catalytic property and hydrothermal stability of Cu-SSZ-13 catalysts for NH₃-SCR, *Appl. Catal. A: Gen.* 550 (2018) 256–265, <https://doi.org/10.1016/j.apcata.2017.11.021>.
 - [18] V. Rizzotto, D. Chen, B.M. Tabak, J.-Y. Yang, D. Ye, U. Simon, P. Chen, Spectroscopic identification and catalytic relevance of NH₄⁺ intermediates in selective NO_x reduction over Cu-SSZ-13 zeolites, *Chemosphere* 250 (2020), 126272, <https://doi.org/10.1016/j.chemosphere.2020.126272>.
 - [19] F. Gao, N.M. Washton, Y. Wang, M. Kollár, J. Szanyi, C.H.F. Peden, Effects of Si/Al ratio on Cu/SSZ-13 NH₃-SCR catalysts: Implications for the active Cu species and the roles of Brønsted acidity, *J. Catal.* 331 (2015) 25–38, <https://doi.org/10.1016/j.jcat.2015.08.004>.
 - [20] R. Daya, Ch.J. Keturakis, D. Trandal, A. Kumar, S.Y. Joshi, A. Yezerets, Alternate pathway for standard SCR on Cu zeolites with gas-phase ammonia, *React. Chem. Eng.* 6 (2021) 1042–1052, <https://doi.org/10.1039/D1RE00041A>.
 - [21] M. Moreno-González, R. Millán, P. Concepción, T. Blasco, M. Boronat, Spectroscopic evidence and Density Functional Theory (DFT) analysis of low-temperature oxidation of Cu⁺ to Cu²⁺/NO_x in Cu-CHA catalysts: Implications for the SCR-NO_x reaction mechanism, *ACS Catal.* 9 (2019) 2725–2738, <https://doi.org/10.1021/acscatal.8b04717>.
 - [22] F. Gao, D. Mei, Y. Wang, J. Szanyi, C.H. Peden, Selective catalytic reduction over Cu/SSZ-13: Linking homo- and heterogeneous catalysis, *J. Am. Chem. Soc.* 139 (2017) 4935–4942, <https://doi.org/10.1021/jacs.7b01128>.
 - [23] C. Paolucci, I. Khurana, A.A. Parekh, S. Li, A.J. Shih, H. Li, J.R. Di Iorio, J. D. Albarracín-Caballero, A. Yezerets, J.T. Miller, W.N. Delgass, F.H. Ribeiro, W. F. Schneider, R. Gounder, Dynamic multinuclear sites formed by mobilized copper ions in NO_x selective catalytic reduction, *Science* 357 (2017) 898–903, <https://doi.org/10.1126/science.aan5630>.
 - [24] T. Anggara, Ch. Paolucci, W.F. Schneider, Periodic DFT characterization of NO_x adsorption in Cu-exchanged SSZ-13 zeolite catalysts, *J. Phys. Chem. C* 120 (2016) 27934–27943, <https://doi.org/10.1021/acs.jpcc.6b07972>.
 - [25] S.A. Bates, W.N. Delgass, F.H. Ribeiro, J.T. Miller, R. Gounder, Methods for NH₃ titration of Brønsted acid sites in Cu-zeolites that catalyze the selective catalytic reduction of NO_x with NH₃, *J. Catal.* 312 (2014) 26–36, <https://doi.org/10.1016/j.jcat.2013.12.020>.
 - [26] H. Kubota, T. Toyao, Z. Maeno, Y. Inomata, T. Murayama, N. Nakazawa, S. Inagaki, Y. Kubota, K. Shimizu, Analogous mechanistic features of NH₃-SCR over vanadium oxide and copper zeolite catalysts, *ACS Catal.* 11 (2021) 11180–11192, <https://doi.org/10.1021/acscatal.1c02860>.
 - [27] A.A. Verma, S.A. Bates, T. Anggara, Ch. Paolucci, A.A. Parekh, K. Kamasamudram, A. Yezerets, J.T. Miller, W.N. Delgass, W.F. Schneider, F.H. Ribeiro, NO oxidation: a probe reaction on Cu-SSZ-13, *J. Catal.* 312 (2014) 179–190, <https://doi.org/10.1016/j.jcat.2014.01.017>.
 - [28] J. Du, Y. Shan, Y. Sun, M. Gao, Z. Liu, X. Shi, Y. Yu, H. He, Unexpected increase in low-temperature NH₃-SCR catalytic activity over Cu-SSZ-39 after hydrothermal aging, *Appl. Catal. B: Environ.* 294 (2021), 120237, <https://doi.org/10.1016/j.apcatb.2021.120237>.
 - [29] F. Gao, E.D. Walter, N.M. Washton, J. Szanyi, C.H.F. Peden, Synthesis and evaluation of Cu/SAPO-34 catalysts for NH₃-SCR 2: Solid-state ion exchange and one-pot synthesis, *Appl. Catal. B: Environ.* 162 (2015) 501–514, <https://doi.org/10.1016/j.apcatb.2014.07.029>.
 - [30] Y. Ma, S. Cheng, X. Wu, Y. Shi, L. Cao, L. Liu, R. Ran, Z. Si, J. Liu, D. Weng, Low-temperature solid-state ion-exchange method for preparing Cu-SSZ-13 selective catalytic reduction catalyst, *ACS Catal.* 9 (2019) 6962–6973, <https://doi.org/10.1021/acscatal.9b01730>.
 - [31] K. Leistner, F. Brüsewitz, K. Wijayanti, A. Kumar, K. Kamasamudram, L. Olsson, Impact of copper loading on NH₃-selective catalytic reduction, oxidation reactions and N₂O formation over Cu/SAPO-34, *Energies* 10 (2017) 489, <https://doi.org/10.3390/en10040489>.
 - [32] A. Jankowska, A. Chlopek, A. Kowalczyk, M. Rutkowska, M. Michalik, S. Liu, L. Chmielarz, Catalytic performance of spherical MCM-41 modified with copper and iron as catalysts of NH₃-SCR process, *Molecules* 25 (2020) 5651, <https://doi.org/10.3390/molecules25235651>.
 - [33] J. Guo, W. Yang, Y. Zhang, L. Gan, Ch. Fan, J. Chen, Y. Peng, J. Li, A multiple-active-site Cu/SSZ-13 for NH₃-SCO: Influence of Si/Al ratio on the catalytic performance, *Catal. Commun.* 135 (2020), 105751, <https://doi.org/10.1016/j.catcom.2019.105751>.
 - [34] F. Han, M. Yuan, S. Mine, H. Sun, H. Chen, T. Toyao, M. Matsuoka, K. Zhu, J. Zhang, W. Wang, T. Xue, Formation of highly active superoxide sites on CuO nanoclusters encapsulated in SAPO-34 for catalytic selective ammonia oxidation, *ACS Catal.* 9 (2019) 10398–10408, <https://doi.org/10.1021/acscatal.9b02975>.
 - [35] J. Wang, Y. Huang, T. Yu, S. Zhu, M. Shen, W. Lic, J. Wang, The migration of Cu species over Cu-SAPO-34 and its effect on NH₃ oxidation at high temperature, *Catal. Sci. Technol.* 4 (2014) 3004–3012, <https://doi.org/10.1039/C4CY00451E>.
 - [36] H. Sjövall, R.J. Blint, L. Olsson, Detailed kinetic modeling of NH₃ and H₂O adsorption, and NH₃ oxidation over Cu-ZSM, -5, *J. Phys. Chem. C* 113 (2009) 1393–1405, <https://doi.org/10.1021/jp802449s>.
 - [37] Ch. Paolucci, A.A. Parekh, I. Khurana, J.R. Di Iorio, H. Li, J.D. Albarracín Caballero, A.J. Shih, T. Anggara, W.N. Delgass, J.T. Miller, F.H. Ribeiro, R. Gounder, W. F. Schneider, Catalysis in a cage: Condition-dependent speciation and dynamics of exchanged Cu cations in SSZ-13 zeolites, *J. Am. Chem. Soc.* 138 (2016) 6028–6048, <https://doi.org/10.1021/jacs.6b02651>.
 - [38] S. Li, Y. Zheng, F. Gao, J. Szanyi, W.F. Schneider, Experimental and computational interrogation of fast SCR mechanism and active sites on H-form SSZ-13, *ACS Catal.* 7 (2017) 5087–5096, <https://doi.org/10.1021/acscatal.7b01319>.
 - [39] N. Usberti, F. Gramigni, N.D. Nasello, U. Iacobone, T. Selli, W. Hu, S. Liu, X. Gao, I. Nova, E. Tronconi, An experimental and modelling study of the reactivity of adsorbed NH₃ in the low temperature NH₃-SCR reduction half-cycle over a Cu-CHA catalyst, *Appl. Catal. B: Environ.* 279 (2020), 119397, <https://doi.org/10.1016/j.apcatb.2020.119397>.
 - [40] K. Liu, Z. Yan, W. Shan, Y. Shan, X. Shi, H. He, Quantitative determination of the Cu species, acid sites and NH₃-SCR mechanism on Cu-SSZ-13 and H-SSZ-13 at low temperatures, *Catal. Sci. Technol.* 10 (2020) 1135–1150, <https://doi.org/10.1039/C9CY02352F>.
 - [41] W.P. Partridge, S.Y. Joshi, J.A. Pihl, N.W. Currier, New operando method for quantifying the relative half-cycle rates of the NO SCR redox cycle over Cu-exchanged zeolites, *Appl. Catal. B: Environ.* 236 (2018) 195–204, <https://doi.org/10.1016/j.apcatb.2018.04.071>.
 - [42] A. Marberger, A.W. Petrov, P. Steiger, M. Elsener, O. Kröcher, M. Nachttegaal, D. Ferril, Time-resolved copper speciation during selective catalytic reduction of NO on Cu-SSZ-13, *Nat. Catal.* 1 (2018) 221–227, <https://doi.org/10.1038/s41929-018-0032-6>.
 - [43] P. Boron, L. Chmielarz, B. Gil, B. Marszałek, S. Dzwigaj, Experimental evidence of the Cu species, acid sites and NH₃-SCR mechanism on Cu-SSZ-13 and H-SSZ-13 at low temperatures, *Appl. Catal. B: Environ.* 198 (2016) 457–470, <https://doi.org/10.1016/j.apcatb.2016.06.012>.
 - [44] S. Kieger, G. Delahay, B. Coq, B. Neveu, Selective catalytic reduction of nitric oxide by ammonia over Cu-FAU catalysts in oxygen-rich atmosphere, *J. Catal.* 183 (1999) 267–280, <https://doi.org/10.1006/jcat.1999.2398>.
 - [45] Y. Miao, L.-D. Chen, Y. He, T. Kuo, Study of SCR cold-start by energy method, *Chem. Eng. J.* 155 (2009) 260–265, <https://doi.org/10.1016/j.cej.2009.07.054>.
 - [46] G. Pétaud, S. Gil, A. Giroir-Fendler, M. Tayakout-Fayolle, Development of a nonequilibrium multisite kinetic model for NH₃-SCR of NO_x on CHA Cu-SAPO-34: Impact of active site configurations and locations, *Ind. Eng. Chem. Res.* 59 (2020) 15848–15864, <https://doi.org/10.1021/acs.iecr.0c02270>.
 - [47] D.W. Fickel, R.F. Lobo, Copper coordination in Cu-SSZ-13 and Cu-SSZ-16 investigated by variable-temperature XRD, *J. Phys. Chem. C* 114 (2010) 1633–1640, <https://doi.org/10.1021/jp9105025>.
 - [48] J. Dedecek, V. Balgova, V. Pashkova, P. Klein, B. Wichterlová, Synthesis of ZSM-5 zeolites with defined distribution of Al atoms in the framework and multinuclear MAS NMR analysis of the control of Al distribution, *Chem. Mater.* 24 (2012) 3231–3239, <https://doi.org/10.1021/cm301629a>.
 - [49] B. Mozgawa, F. Zasada, M. Fedyna, K. Góra-Marek, E. Tabor, K. Mlekodaj, J. Dedecek, Z. Zhao, P. Pietrzyk, Z. Sojka, Analysis of NH₃-TPD profiles for CuSSZ-13 catalyst of controlled Al distribution – complexity resolved by first principles thermodynamics of NH₃ desorption, IR and EPR insight into Cu speciation, *Chem. Eur. J.* 27 (2021) 17159–17186, <https://doi.org/10.1002/chem.202102790>.
 - [50] K. Góra-Marek, A.E. Palomares, A. Glanowska, K. Sadowska, J. Datka, Copper sites in zeolites - quantitative IR studies, *Microporous Mesoporous Mater.* 162 (2012) 175–180, <https://doi.org/10.1016/j.micromeso.2012.06.029>.
 - [51] T. Spalek, P. Pietrzyk, Z. Sojka, Application of the genetic algorithm joint with the Powell method to nonlinear least-squares fitting of powder EPR spectra, *J. Chem. Inf. Model.* 45 (2005) 18–29, <https://doi.org/10.1021/ci049863s>.
 - [52] A.K. Mishra, A. Roldan, N.H. De Leeuw, CuO surfaces and CO₂ activation: a dispersion-corrected DFT, U Study, *J. Phys. Chem. C* 120 (2016) 2198–2214, <https://doi.org/10.1021/acs.jpcc.5b10431>.
 - [53] P. Raybaud, D. Costa, M.C. Valero, C. Arrouvel, M. Digne, P. Sautet, H. Toulhoat, First principles surface thermodynamics of industrial supported catalysts in working conditions, *J. Phys.: Condens. Matter* 20 (2008), 064235, <https://doi.org/10.1088/0953-8984/20/6/064235>.
 - [54] F. Giordanino, P.N.R. Vennestrom, L.F. Lundegaard, F.N. Stappen, S. Mossin, P. Beato, S. Bordiga, C. Lamberti, Characterization of Cu-exchanged SSZ-13: a comparative FTIR, UV-Vis, and EPR study with Cu-ZSM-5 and Cu-β with similar Si/Al and Cu/Al ratios, *Dalton Trans.* 42 (2013) 12741–12761, <https://doi.org/10.1039/C3DT50732G>.
 - [55] C.J. Van Oers, K. Góra-Marek, B. Prelot, J. Datka, V. Meynen, P. Cool, Demonstrating the benefits and pitfalls of various acidity characterization techniques by a case study on bimodal aluminosilicates, *Langmuir* 30 (2014) 1880–1887, <https://doi.org/10.1021/la4034194>.
 - [56] H. Zhang, J. Lv, Z. Zhang, C. Du, S. Wang, J. Lin, S. Wan, Y. Wang, H. Xiong, Oxidation of methane to methanol by water over Cu/SSZ-13: Impact of Cu loading and formation of active sites, *ChemCatChem* 14 (2022), e202101609, <https://doi.org/10.1002/cctc.202101609>.
 - [57] Y. Ma, X. Wu, J. Ding, L. Liu, B. Jin, E.D. Walter, R. Ran, Z. Si, F. Gao, D. Weng, Quasi-operando quantification of Cu(II) ions in Cu-SSZ-13 catalyst by an NH₃ temperature programmed reduction method, *Chem. Commun.* 57 (2021) 1891–1895, <https://doi.org/10.1039/D0CC07346F>.
 - [58] C. Liu, G. Malta, H. Kubota, T. Toyao, Z. Maeno, K. Shimizu, Mechanism of NH₃-selective catalytic reduction (SCR) of NO/NO₂ (fast SCR) over Cu-CHA zeolites studied by in situ/operando infrared spectroscopy and density functional theory, *J. Phys. Chem. C* 125 (2021) 21975–21987, <https://doi.org/10.1021/acs.jpcc.1c06651>.
 - [59] C. Liu, G. Malta, H. Kubota, T. Toyao, Z. Maeno, K. Shimizu, Mechanism of NH₃-selective catalytic reduction (SCR) of NO/NO₂ (fast SCR) over Cu-CHA zeolites studied by in situ/operando infrared spectroscopy and density functional theory, *J. Phys. Chem. C* 125 (2021) 21975–21987, <https://doi.org/10.1021/acs.jpcc.1c06651>.

- [60] Ch Negri, E. Borfecchia, M. Cutini, K.A. Lomachenko, T.V.W. Janssens, G. Berlier, S. Bordiga, Evidence of mixed-ligand complexes in Cu-CHA by reaction of Cu nitrates with NO/NH₃ at low temperature, *ChemCatChem* 11 (2019) 3828–3838, <https://doi.org/10.1002/cctc.201900590>.
- [61] N.S. Gupta, S. Basu, P. Payra, P. Mathur, S. Bhaduri, G.K. Lahiri, Reduction of nitrite to NO in an organised triphasic medium by platinum carbonyl clusters and redox active dyes as electron carriers, *Dalton Trans.* (2007) 2594–2598, <https://doi.org/10.1039/b703352d>.
- [62] Y. Mao, Z. Wang, H.-F. Wang, P. Hu, Understanding catalytic reactions over zeolites: a Density Functional Theory study of selective catalytic reduction of NO_x by NH₃ over Cu-SAPO-34, *ACS Catal.* 6 (2016) 7882–7891, <https://doi.org/10.1021/acscatal.6b01449>.
- [63] G. Centi, S. Perathoner, D. Biglino, E. Giamello, Adsorption and reactivity of NO on copper-on-alumina catalysts: I. Formation of nitrate species and their influence on reactivity in NO and NH₃ conversion, *J. Catal.* 152 (1995) 75–92, <https://doi.org/10.1006/jcat.1995.1062>.
- [64] K. Hadjiivanov, J. Saussey, J.L. Freysz, J.C. Lavalley, FT-IR study of NO + O₂ co-adsorption on H-ZSM-5: re-assignment of the 2133cm⁻¹ band to NO⁺ species, *Catal. Lett.* 52 (1998) 103–108, <https://doi.org/10.1023/A:1019059117488>.
- [65] C. Liu, S. Yasumura, T. Toyao, Z. Maeno, K. Shimizu, Mechanism of standard NH₃-SCR over Cu-CHA via NO⁺ and HONO intermediates, *J. Phys. Chem. C* 126 (2022) 11594–11601, <https://doi.org/10.1021/acs.jpcc.2c03432>.
- [66] L. Negahdar, N.E. Omori, M.G. Quesne, M.D. Frogley, F. Cacho-Nerin, W. Jones, S. W.T. Price, C.R.A. Catlow, A.M. Beale, Elucidating the significance of copper and nitrate speciation in Cu-SSZ-13 for N₂O formation during NH₃-SCR, *ACS Catal.* 11 (2021) 13091–13101, <https://doi.org/10.1021/acscatal.1c03174>.
- [67] J.R. Di Iorio, S.A. Bates, A.A. Verma, W.N. Delgass, F.H. Ribeiro, J.T. Miller, R. Gounder, The dynamic nature of Brønsted acid sites in Cu-zeolites during NO_x selective catalytic reduction: quantification by gas-phase ammonia titration, *Top. Catal.* 58 (2015) 424–434, <https://doi.org/10.1007/s11244-015-0387-8>.
- [68] S.A. Bates, A.A. Verma, Ch Paolucci, A.A. Parekh, T. Anggara, A. Yezerets, W. F. Schneider, J.T. Millere, W.N. Delgass, F.H. Ribeiro, Identification of the active Cu site in standard selective catalytic reduction with ammonia on Cu-SSZ-13, *J. Catal.* 312 (2014) 87–97, <https://doi.org/10.1016/j.jcat.2014.01.004>.
- [69] B. Kerkeni, D. Berthout, D. Berthomieu, D.E. Doronkin, M. Casapu, J.-D. Grunwaldt, C. Chizallet, Copper coordination to water and ammonia in Cu^{II}-exchanged SSZ-13: atomistic insights from DFT calculations and in situ XAS experiments, *J. Phys. Chem. C* 122 (2018) 16741–16755, <https://doi.org/10.1021/acs.jpcc.8b03572>.
- [70] M.P. Ruggeri, T. Sella, M. Colombo, I. Nova, E. Tronconi, Identification of nitrites/HONO as primary products of NO oxidation over Fe-ZSM-5 and their role in the standard SCR mechanism: a chemical trapping study, *J. Catal.* 311 (2014) 266–270, <https://doi.org/10.1016/j.jcat.2013.11.028>.
- [71] Y. Feng, X. Wang, T.V.W. Janssens, P.N.R. Venneström, J. Jansson, M. Skoglundh, H. Grönbeck, First-principles microkinetic model for low-temperature NH₃-assisted selective catalytic reduction of NO over Cu-CHA, *ACS Catal.* 11 (2021) 14395–14407, <https://doi.org/10.1021/acscatal.1c03973>.
- [72] C. Liu, G. Malta, H. Kubota, T. Toyao, Z. Maeno, K. Shimizu, Mechanism of NH₃-selective catalytic reduction (SCR) of NO/NO₂ (fast SCR) over Cu-CHA zeolites studied by in situ/operando infrared spectroscopy and density functional theory, *J. Phys. Chem. C* 125 (2021) 21975–21987, <https://doi.org/10.1021/acs.jpcc.1c06651>.